

# Solving large-scale MEG/EEG source localization and functional connectivity problems simultaneously using state-space models

Jose M. Sanchez-Bornot<sup>1</sup>, Roberto C. Sotero<sup>2</sup>, Scott Kelso<sup>1,3</sup>, and Damien Coyle<sup>1</sup>

<sup>1</sup> Intelligent Systems Research Centre, School of Computing, Engineering and Intelligent Systems, Ulster University, Magee campus, Derry~Londonderry, UK.

<sup>2</sup> Department of Radiology and Hotchkiss Brain Institute, University of Calgary, Calgary, AB, Canada.

<sup>3</sup> Center for Complex Systems and Brain Sciences, Florida Atlantic University, Boca Raton, Florida.

## Highlights

1. We propose multiple penalized state-space (MPSS) models to solve MEG/EEG source localization and functional connectivity problems simultaneously.
2. We propose backpropagation and state-space gradient descent algorithms as straightforward solutions to solve MPSS models, particularly for small-scale scenarios.
3. An alternating least squares (ALS) algorithm, based on closed-form iterative solutions, is devised to solve MPSS models much more efficiently for large-scale scenarios, e.g., for thousands of brain dipole sources.
4. We propose an extension of  $K$ -fold cross-validation to evaluate an MPSS model's regularisation parameters.
5. We apply the proposed techniques to small- and large-scale simulations and MEG/EEG data.

## Abstract

State-space models are used in many fields when dynamics are unobserved. Popular methods such as the Kalman filter and expectation maximization enable estimation of these models but pay a high computational cost in large-scale analysis. In these approaches, sparse inverse covariance estimators can reduce the cost; however, a trade-off between enforced sparsity and increased estimation bias occurs, which demands careful consideration in low signal-to-noise ratio scenarios. We overcome these limitations by 1) Introducing multiple penalized state-space models based on data-driven regularization; 2) Implementing novel algorithms such as backpropagation, state-space gradient descent, and alternating least squares; 3) Proposing an extension of  $K$ -fold cross-validation to evaluate the regularization parameters. Finally, we solve the simultaneous brain source localization and functional connectivity problems for simulated and real MEG/EEG signals for thousands of sources on the cortical surface, demonstrating a substantial improvement over state-of-the-art methods.

## Introduction

Solving magneto/encephalographic (MEG/EEG) source localization and functional connectivity (FC) problems are active research areas as they can improve our understanding of the information processing of spontaneous or evoked events in human brains<sup>1</sup>. Although the information processing usually relies on the localized activations of brain regions involved in memory recalling and the analysis of visual, auditory, language, sensorimotor, and other critical information, these activations are created and synchronized through short- (e.g., intraregional) and long-range (interregional) communication networks, e.g., attentional and default-mode networks<sup>2</sup>. Two critical steps to identify and study the information-processing pathways are (1) to improve the methods for brain

source localization and (2) to increase the accuracy in estimation and identification of functionally connected networks. These steps are fundamental to understanding human intelligence as an emerging property of the integration and segregation of information through brain networks and may guide the development of new methods to build Artificial Intelligence (AI).

MEG/EEG and electrocorticogram (ECoG) are among the most appropriate neuroimaging techniques to study neuronal dynamics because they can track brain activity with millisecond resolution<sup>1</sup>. Although these techniques present limitations due to their invasiveness (ECoG) or recording outside the scalp (MEG/EEG), we consider that the main shortcomings are in the analytical tools used to derive information from these signals. For example, most established methods to map brain activity are applied only to a few regions of interest (ROI) or small-scale scenarios due to the high computational cost, such as seen in expectation maximization (EM) implementations to solve dynamic causal models (DCMs)<sup>3</sup>, and in general EM and Kalman filter applications to solve state-space models<sup>4-10</sup>. However, discarding the high-dimensional content of brain dynamics may produce spurious results due to ignored cause-effect relationships<sup>11</sup>. Furthermore, the typical brain source localization<sup>12-18</sup> and FC<sup>19-21</sup> approaches mainly contemplate the solution of these problems separately, without considering that they must constrain each other<sup>22-25</sup>. Although state-space models address this concern<sup>4,7,8</sup>, unfortunately, only a few studies have dealt with large-scale analysis<sup>10</sup>.

Moreover, FC analyses may be biased if based directly on MEG/EEG sensor data as is regularly the case<sup>6,21,26,27</sup>, because of volume conduction<sup>21,26</sup>. Biasness may also arise in FC analyses based on fMRI measurements as is the case in resting-state FC studies (rs-fcMRI)<sup>28-30</sup>, because fMRI provides high spatial localization at the expense of low temporal resolution<sup>31,32</sup>. Furthermore, even those FC analysis based directly on the information extracted from brain sources can be biased if a short-sighted approach was used to extract the source information, e.g., methods that reduce dimensions such as in ROI analysis<sup>11,33,34</sup>. Nowadays, with the emergence of Big Data Analytics<sup>35</sup> and high-performance computing (HPC) tools, such reductionist approaches must be disregarded. However, few neuroimaging studies are exploiting the HPC tools that are critical to deal with large-scale analysis<sup>10,33</sup>.

On the contrary, large-scale analyses are universal in training artificial neural networks (ANNs), or deep learning, where methods deal with overfitting and ill-posed problems with more practical approaches. Current research on ANNs extensively uses backpropagation algorithms<sup>36-39</sup> due to their simple mathematical and computational representations. Although training ANNs with backpropagation may differ from how the brain learns and encodes information<sup>40,41</sup>, brain sciences and ANNs could benefit from cross-disciplinary research<sup>40-43</sup>.

To address the limitations above, the main goals of our study are twofold: 1) To develop a novel methodology to solve state-space models (**Figs. 1A-E**) in different signal-to-noise ratio (SNR) scenarios, and 2) To solve MEG/EEG source localization and FC problems simultaneously (**Figs. 1F-G**). For the first goal, we initially propose a simple backpropagation algorithm to solve state-space models (**Fig. 1B**). This application is only possible using the weight decay<sup>42</sup> technique applied in deep learning to deal with noisy signals as justified from a Bayesian standpoint. After that, we use a Bayesian framework to introduce more general multiple penalized state-space (MPSS) models. Moreover, we propose a state-space gradient descent (SSGD) algorithm (**Fig. 1C**) to more robustly solve MPSS models than backpropagation. Due to the quadratic nature of our optimization problem, we also propose an alternating least-squares (ALS) algorithm (**Fig. 1D**) with much faster convergence for large-scale analysis. Another critical contribution of this research is introducing an extension of  $K$ -fold cross-validation to estimate the regularization parameters in MPSS models (**Fig. 1E**). For the

second goal, we apply this methodology to estimate large-scale brain sources dynamics and their FC for simulated MEG data, providing ground truth for testing the accuracy of estimated spatiotemporal components and FC maps. Finally, we examine a single-subject MEG/EEG data for a familiar faces recognition task as a proof of concept. Our methodology significantly improves the state-of-the-art and introduces more comprehensive and straightforward solutions to state-space models.

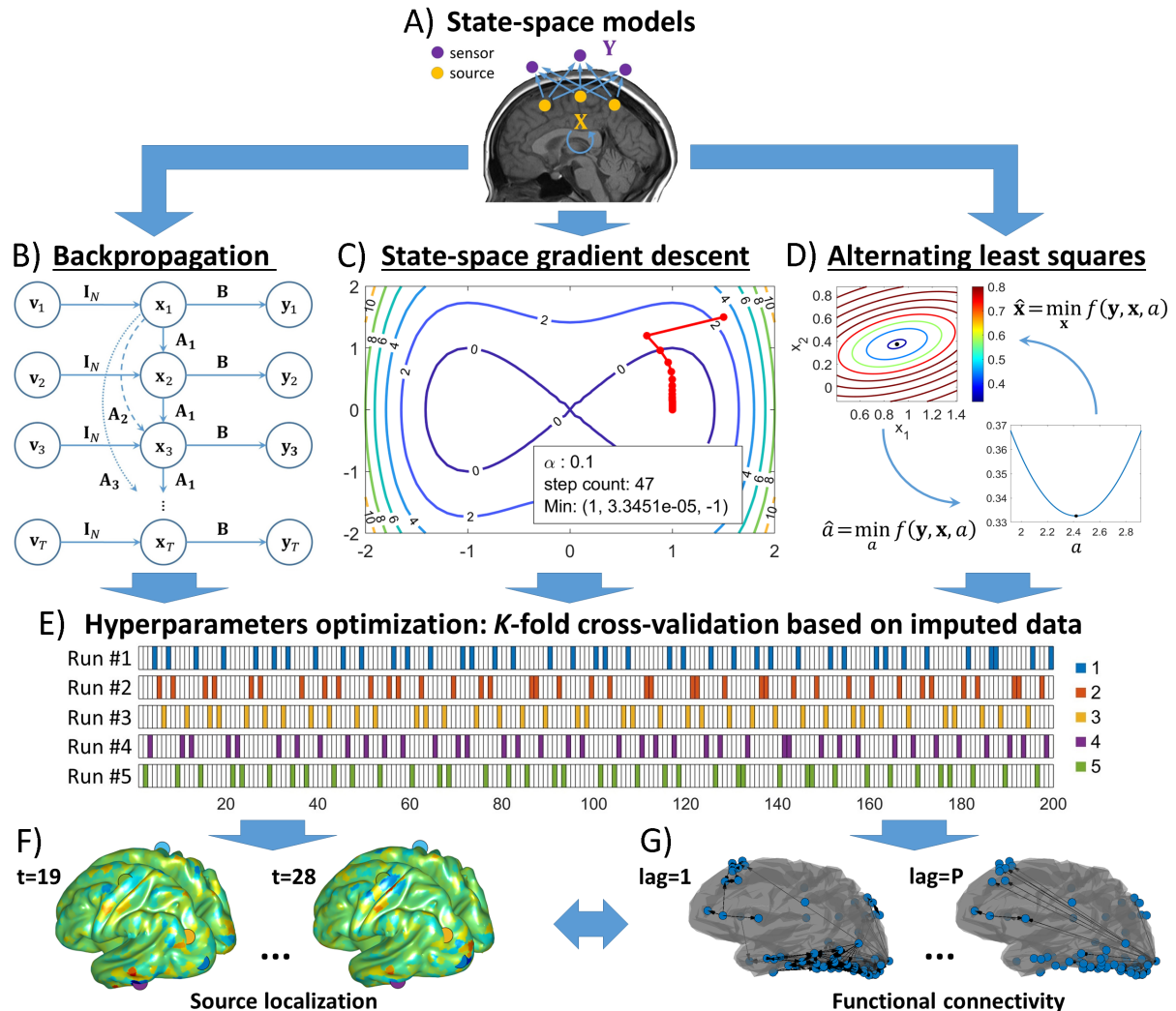


**Figure 1:** Solving a state-space model with more general multiple penalized data-driven regularization approaches. (A) The model represents the generation of MEG/EEG data from the dynamical changes of neurons' activity and communication, e.g., as in Eqs. (1, 2). Particularly, only the variables  $y_1, \dots, y_T$  can be observed, i.e., sensors measurements, whereas the hidden state variables  $x_1, \dots, x_T$  represent the neuronal dynamics, and the circular self-referencing arrow indicates the lagged neural connections, e.g.  $A_1, \dots, A_p$  in the equations. (B) Graphical representation of the data generation using the state-space model in Eqs. (1, 2). The graph also corresponds to the forward propagation stage of the proposed backpropagation algorithm. Particularly, it represents the interactions for lag=1,2,3 delayed influences from the past to produce the present dynamics. The added observation noise vectors  $w_1, \dots, w_T$  are not represented in the diagram for simplicity, whereas the state noise vectors  $v_1, \dots, v_T$  are represented as input vectors multiplied by the identity operator  $I_N \in \mathcal{R}^{N \times N}$ . (C) Local optimization of the model using a proposed state-space gradient descent (SSGD) algorithm. Both SSGD and backpropagation depend on selecting the gradient descent step size and momentum. (D) Proposed alternating least squares (ALS) algorithm which offers more efficient iteratively closed-form solutions to the model, particularly for large-scale analysis. (E) Proposed extension of classical K-fold cross-validation based on imputed data from the model, enabling selection of the "optimal" regularization parameters used during the model parameter estimation with proposed algorithms. (F-G) This methodology enables the simultaneous solution of brain source localization and functional connectivity problems.

## Results

### Backpropagation solution for a classical state-space model

Instead of using probabilistic approaches such as in Kalman filter and EM, we derived and tested a backpropagation algorithm for the state-space model:

$$\mathbf{y}_t = \mathbf{B}\mathbf{x}_t + \mathbf{w}_t; \text{ with } \mathbf{w}_t \sim \text{MGD}(0, \sigma_o^2 \mathbf{I}_M); t = 1, 2, \dots, T, \quad (1)$$

$$\mathbf{x}_t = \sum_{p=1}^P \mathbf{A}_p \mathbf{x}_{t-p} + \mathbf{v}_t; \text{ with } \mathbf{v}_t \sim \text{MGD}(0, \sigma_s^2 \mathbf{I}_N); t = P + 1, \dots, T, \quad (2)$$

where we represented the state dynamics  $\mathbf{x}_t \in \mathcal{R}^{N \times 1}$  (column vector), for  $t = 1, 2, \dots, T$  time instants, using the multivariate autoregressive (MVAR) equation (**Eq. (2)**). For example, the MVAR generative model can produce surrogate data for the neuronal activity in  $N$  spatial locations of the brain, while the MVAR's coefficients  $\mathbf{A}_p \in \mathcal{R}^{N \times N}$ ,  $p = 1, \dots, P$ , represent the surrogate neuronal communication for lagged (lag= $p$ ) interactions. Correspondingly, the observed dynamics  $\mathbf{y}_t \in \mathcal{R}^{M \times 1}$  represent  $M$ -variate measurements (time-series) obtained from the MEG/EEG sensors (**Eq. (1)**), and  $\mathbf{B} \in \mathcal{R}^{M \times N}$  is the mixing (leadfield) matrix. The state-space model also includes noise terms  $\mathbf{v}_t \in \mathcal{R}^{N \times 1} \sim N(0, \sigma_s^2 \mathbf{I}_N)$  and  $\mathbf{w}_t \in \mathcal{R}^{M \times 1} \sim N(0, \sigma_o^2 \mathbf{I}_M)$  to account for the perturbation in state and observation dynamics, respectively. For simplicity, noise terms are assumed to be independent (i.i.d.) and follow multivariate normal distributions with variances  $\sigma_o^2$  and  $\sigma_s^2$ .

**Figs. 1A-B** show an application and a graphical representation for a state-space model. Notice that the graph resembles the diagram of unrolled recurrent neural networks (RNNs), i.e., for the application of backpropagation through time algorithms<sup>36,41</sup>, in which the MVAR's coefficients play a similar role to the shared weights in RNNs. The only known data to solve this problem are the observations  $\mathbf{y}_t$ , while  $\mathbf{x}_t$  and  $\mathbf{A}_p$  are the model parameters. From the analogy with RNNs, this graph helps to derive a backpropagation algorithm for the general case when considering several delayed influences. Backpropagation enables the estimation of  $\mathbf{A}_p$  and  $\mathbf{v}_t$  directly and uses the MVAR's equation to generate the time series  $\mathbf{x}_t$  from these estimates during the forward propagation phase (**Extended Data Table 1**). We implement backpropagation using gradient descent (GD) with the momentum modification<sup>42</sup> (see **Online Methods**), which improves the algorithm's convergence in our analysis.

Next, we tested the backpropagation accuracy with our study's most simple small-scale simulation. The simulation was created for  $T = 200$ ,  $M = 5$ ,  $N = 2$ , and  $P = 1$ , by controlling the SNR using  $\sigma_o = 0.1$ ,  $\sigma_o = 0.5$ , and  $\sigma_o = 1$ . By setting  $\sigma_s = 1$  and  $\mathbf{A}_1 = \begin{pmatrix} -0.5 & 0 \\ 0.7 & -0.5 \end{pmatrix}$ , we generate  $\mathbf{x}_t$  and  $\mathbf{y}_t$  randomly using **Eqs. (1, 2)**. In general, the simulated  $\mathbf{x}_t$  and  $\mathbf{A}_p$  serve as ground truth to compare the accuracy of the algorithms. We use a numerical tolerance of  $10^{-6}$  as convergence criteria unless otherwise stated.

For this simulation, backpropagation converges as tested for several random replications. For nearly noiseless ( $\sigma_o = 0.1$ ) scenarios, it always recovers solutions nearby the ground truth. For example, using the relative squared error formula,  $RSE = \frac{\sum_{t=1}^T (x_t - \hat{x}_t)^2}{\sum_{t=1}^T (x_t - \bar{x})^2}$  where  $\bar{x} = \frac{1}{T} \sum_{t=1}^T x_t$ , the accuracy of the estimated bivariate time series  $\hat{\mathbf{x}}_t$  are approximately 0.014 and 0.004 for  $\sigma_o = 0.1$  (algorithm converges after 130,947 iterations, with GD step  $\alpha = 1$ , momentum  $\mu = 0.99$ ), 0.177 and 0.071 for  $\sigma_o = 0.5$  (9,867 iterations,  $\alpha = 1$ ,  $\mu = 0.99$ ), and 0.752 and 0.326 for  $\sigma_o = 1$  (5,564 iterations,  $\alpha = 1$ ,  $\mu = 0.99$ ).

Notice that the error increases dramatically for low SNR, which may be a sign of overfitting. This trend occurs despite the backpropagation implementation using the weight decay technique, with

$\lambda = \sigma_o^2 / \sigma_s^2$  as recommended using the Bayesian criteria for the known probabilistic distributions. Otherwise, ignoring weight decay is equivalent to fitting the model disregarding the noise in the data. **Table 1** shows the outcome for the estimated autoregressive coefficients for each case, with similar increased bias as SNR decreases. We also noted that backpropagation is sensitive to the tuning of the algorithm. Without momentum, it converges to the same solution but much slower as we had to set  $\alpha = 0.01$  due to numerical instability.

**Table 1:** Backpropagation solutions for one replication of the most straightforward ( $N = 2$  sources and lag=1) small-scale simulation for each SNR scenario, using **Eqs. (1, 2)**. The values of simulation parameters are  $T = 200$ ,  $M = 5$ ,  $N = 2$ , and  $P = 1$ . From left to right are shown the ground-truth values of the autoregressive matrix, together with the corresponding solutions for  $\sigma_o = 0.1$ ,  $\sigma_o = 0.5$ , and  $\sigma_o = 1$ . We set  $\sigma_s = 1$  in all simulations.

| Ground truth   | backprop: $\sigma_o = 0.1$   | backprop: $\sigma_o = 0.5$  | backprop: $\sigma_o = 1$   |
|--|--|---|--|
| $\begin{pmatrix} -0.5 & 0 \\ 0.7 & -0.5 \end{pmatrix}$ | $\begin{pmatrix} -0.5016 & 0.0159 \\ 0.7574 & -0.4012 \end{pmatrix}$ | $\begin{pmatrix} -0.6301 & -0.0123 \\ 1.1034 & -0.3353 \end{pmatrix}$ | $\begin{pmatrix} -0.4849 & -0.0064 \\ 5.3297 & 0.0520 \end{pmatrix}$ |

### Multiple penalized state-space (MPSS) models

State-space models can also be examined from a Bayesian perspective by considering probability distributions to represent the state and observation dynamics (see **Eqs. (5-7)** in **Online Methods**) and incorporate *a priori* information that may enhance the estimators' stability. For example, our use of weight decay in backpropagation is enabled by conditional and *a priori* distributions (**Eqs. (6, 7)**). Additionally, we could assume that MVAR's coefficients follow *a priori* a multivariate normal distribution, i.e.,  $\text{vec}(\mathbf{A}_p) \sim N(\mathbf{0}_{N^2}, \sigma_{2,\alpha}^2 \mathbf{I}_{N^2})$ , using the vectorization operator  $\text{vec}()$ , which leads to an  $\ell_2$ -norm based regularization approach. Other distributions could also be considered, such as the Laplace distribution, i.e.,  $\text{vec}(\mathbf{A}_p) \sim \text{Laplace}(\mathbf{0}_{N^2}, \sigma_{1,\alpha}^2 \mathbf{I}_{N^2})$ , which leads to  $\ell_1$ -norm regularization. We can generally consider a mixture of *a priori* distributions that may include information for other variables, e.g.,  $\mathbf{x}_t \sim \text{Laplace}(\mathbf{0}, \sigma_{1,x}^2 \mathbf{I}_N)$ . These statistical designs are widely considered in inverse problems, as shown by MUSIC, LORETA, and other methods<sup>17,44</sup>.

Here, we propose MPSS models as a more general formulation of state-space models designed for large-scale analysis, using the optimization problem:

$$F = \frac{1}{2T} \left\{ \sum_{t=1}^T \|\mathbf{y}_t - \mathbf{B}\mathbf{x}_t\|_2^2 + \lambda \sum_{t=p+1}^T \|\mathbf{x}_t - \sum_{p=1}^P \mathbf{A}_p \mathbf{x}_{t-p}\|_2^2 \right\} + \lambda \sum_{t=1}^P \|\mathbf{x}_t\|_2^2 + \lambda_2^{(a)} \|\mathbf{A}\|_F^2 + 2\lambda_1^{(x)} \|\mathbf{x}\|_1 + 2\lambda_1^{(a)} \|\mathbf{A}\|_1 \quad (3)$$

$$\hat{\mathbf{x}}, \hat{\mathbf{A}} = \underset{\mathbf{x}, \mathbf{A}}{\text{argmin}} F(\mathbf{x}, \mathbf{y}, \mathbf{A}, \mathbf{B}, \lambda, \lambda_2^{(a)}, \lambda_1^{(x)}, \lambda_1^{(a)}) \quad (4)$$

Realistically, to estimate the parameters  $\mathbf{x}_t$ ,  $t = 1, 2, \dots, T$ , and  $\mathbf{A}_p$ ,  $p = 1, \dots, P$ , we must first find suitable values for the hyperparameters  $\lambda$ ,  $\lambda_2^{(a)}$ ,  $\lambda_1^{(x)}$ , and  $\lambda_1^{(a)}$ . Later, we propose an extension of  $K$ -fold cross-validation to select these values. Otherwise, assuming the conditional and *a priori* distributions are known, we can estimate "naïve" solutions corresponding to  $\lambda = \sigma_o^2 / \sigma_s^2$ ,  $\lambda_2^{(a)} = \sigma_o^2 / \sigma_{2,a}^2$ ,  $\lambda_1^{(x)} = 0.5 \sigma_o^2 / \sigma_{1,x}^2$  and  $\lambda_1^{(a)} = 0.5 \sigma_o^2 / \sigma_{1,a}^2$ .

### State-space gradient descent (SSGD) algorithm to solve MPSS models

To solve MPSS models, we proposed a state-space gradient descent (SSGD) algorithm (**Eqs. (11-13)** in **Online Methods**) as an alternative to backpropagation. SSGD was initially tested with the same simulation and using  $\lambda = \sigma_o^2 / \sigma_s^2$ , as above. We set to zero the other hyperparameters, i.e.,  $\lambda_2^{(a)} = \lambda_1^{(x)} = \lambda_1^{(a)} = 0$ . Unsurprisingly, the algorithm converged to the same solution as backpropagation for the same replication but with faster convergence and more stability (less sensitivity) with the use

of momentum. For example, without momentum ( $\mu = 0$ ), SSGD converged after 6,434 iterations for  $\sigma_o = 0.1$  ( $\alpha = 1$ ), 7,234 iterations for  $\sigma_o = 0.5$  ( $\alpha = 1$ ), and 15,522 iterations for  $\sigma_o = 1$  ( $\alpha = 0.6$ ); with momentum  $\mu = 0.99$ , it converged after 5,391 iterations for  $\sigma_o = 0.1$  ( $\alpha = 1$ ), 6,290 iterations for  $\sigma_o = 0.5$  ( $\alpha = 1$ ), and 8,788 iterations for  $\sigma_o = 1$  ( $\alpha = 1$ ).

To further compare SSGD and backpropagation algorithms, we created another small-scale but more complex simulation, with parameters  $T = 240$ ,  $M = 5$ ,  $N = 3$ , and  $P = 3$  (i.e., lag=1,2,3). The complexity increases because the model involves three hidden ( $N = 3$ ) state variables and three lagged interactions ( $P = 3$ ). Likewise, the data generation uses **Eqs. (1, 2)**, with the ground-truth autoregressive coefficients shown in **Table 2**.

**Table 2:** SSGD solution for estimated autoregressive coefficients for one replication of the more complex ( $N = 3$  sources and lag=1,2,3) small-scale simulation using **Eqs. (1, 2)**. The values of simulation parameters are  $T = 240$ ,  $M = 5$ ,  $N = 3$ , and  $P = 3$ . **(I)** The simulation's ground-truth autoregressive coefficients were obtained according to Stokes and Purdon<sup>45</sup>, presented between brackets (from the left to right) correspondingly to lag=1,2,3, in this order. **(II)** From top to bottom are shown the estimated autoregressive coefficients without using momentum ( $\mu = 0$ ), for  $\sigma_o = 0.1$ ,  $\sigma_o = 0.5$ , and  $\sigma_o = 1$  in this order. We set  $\sigma_s = 1$  in all simulations.

| <b>I) Ground-truth autoregressive coefficients</b>   |  |
|--|--|
| $\mathbf{A} = \left\{ \begin{pmatrix} -0.900 & 0 & 0 \\ -0.356 & 1.2124 & 0 \\ 0 & -0.3098 & -1.3856 \end{pmatrix}, \begin{pmatrix} -0.81 & 0 & 0 \\ 0.7136 & -0.49 & 0 \\ 0 & 0.5 & -0.64 \end{pmatrix}, \begin{pmatrix} 0 & 0 & 0 \\ -0.356 & 0 & 0 \\ 0 & -0.3098 & 0 \end{pmatrix} \right\}$ |  |
| <b>II) Autoregressive coefficients estimated without momentum (<math>\mu = 0</math>)</b>   |  |
| $\sigma_o = 0.1$<br>$\alpha = 1$   | $\mathbf{A} = \left\{ \begin{pmatrix} -1.07 & 0.09 & -0.02 \\ -0.45 & 1.27 & 0.09 \\ -0.04 & -0.36 & -1.44 \end{pmatrix}, \begin{pmatrix} -0.85 & -0.02 & -0.04 \\ 0.62 & -0.46 & 0.14 \\ -0.04 & 0.47 & -0.70 \end{pmatrix}, \begin{pmatrix} -0.13 & -0.06 & -0.03 \\ -0.45 & -0.09 & 0.05 \\ -0.03 & -0.27 & -0.01 \end{pmatrix} \right\}$ |
| $\sigma_o = 0.5$<br>$\alpha = 10^{-2}$   | $\mathbf{A} = \left\{ \begin{pmatrix} -2.39 & -1.83 & 2.01 \\ 1.80 & 4.84 & -3.80 \\ 1.11 & 1.95 & -3.99 \end{pmatrix}, \begin{pmatrix} -2.60 & 3.18 & 3.11 \\ 3.49 & -6.54 & -5.90 \\ 1.41 & -3.69 & -4.61 \end{pmatrix}, \begin{pmatrix} 0.53 & -1.39 & 1.61 \\ -1.98 & 2.58 & -3.11 \\ -1.56 & 1.65 & -2.02 \end{pmatrix} \right\}$       |
| $\sigma_o = 1$<br>$\alpha = 10^{-3}$   | $\mathbf{A} = \left\{ \begin{pmatrix} 1.48 & 4.71 & -5.75 \\ -0.51 & 2.36 & 1.23 \\ 0.87 & -1.27 & -4.46 \end{pmatrix}, \begin{pmatrix} 4.20 & -27.83 & -19.46 \\ 0.49 & -0.45 & 1.62 \\ 0.60 & -6.86 & -7.98 \end{pmatrix}, \begin{pmatrix} -7.01 & 19.35 & -13.53 \\ 0.16 & -0.70 & 0.49 \\ -2.38 & 6.32 & -4.42 \end{pmatrix} \right\}$   |

Similar to the previous analysis, we evaluated the algorithms using  $\sigma_o = 0.1$ ,  $\sigma_o = 0.5$ , and  $\sigma_o = 1$  while fixing  $\sigma_s = 1$ . For the highest SNR scenario, backpropagation and SSGD tend to converge to the ground-truth solutions, but backpropagation convergence was significantly slower and less stable. Henceforth, we only present the SSGD results. For example, for one replication for each SNR level, without momentum ( $\mu = 0$ ) and using the RSE statistic, the SSGD accuracy for the estimation of the three-variate time series  $\mathbf{x}_t$  are approximately 0.004, 0.002, and 0.001, for  $\sigma_o = 0.1$  (8,915 iterations, with  $\alpha = 1$ ), 0.067, 0.042, and 0.018, for  $\sigma_o = 0.5$  (3,671,869 iterations,  $\alpha = 10^{-2}$ ), and 0.327, 0.183, and 0.075 for  $\sigma_o = 1$  (18,715,396 iterations,  $\alpha = 10^{-3}$ ). As for the previous analysis, we also observed that estimator  $\hat{\mathbf{x}}_t$  gradually diverges as SNR decreases. As shown in **Table 2**, the same issue occurred with the estimation of the autoregressive coefficients.

Moreover, for the second simulation, we also had to deal with numerical instabilities that forced us to select smaller values of  $\alpha$  for increasing noisier scenarios. For instance, we obtained a different solution for the noisiest case when selecting  $\alpha = 10^{-2}$  instead of  $10^{-3}$ , with worsened RSE statistic. Notably, we did not test SSGD with momentum in this simulation due to numerical instability, which is more noticeable in calculating the autoregressive coefficients. Reducing the tolerance to  $10^{-7}$  or less may overcome this apparent lack of uniqueness. However, an overshoot of the unique solution can always occur if the algorithm uses a relatively higher value of  $\alpha$ . In the general case, we recommend testing whether a smaller value of  $\alpha$  can produce better results.

## The problem of overfitting in state-space models

In the results above, overfitting was more noticeable mainly for estimating the autoregressive coefficients for the noisier cases of  $\sigma_o = 0.5$  and  $\sigma_o = 1$  as shown in **Tables 1-2**, whereas the corresponding estimated time series  $\hat{\mathbf{x}}_t$  were very stable as shown in **Fig. 2**. Particularly, for the second simulation, it was remarkable that the curves for estimated time series were very close to the ground truth even for low SNR (**Fig. 2B**), as was also noted from the reported RSE statistics above. However, this stability on the time series estimation can also degrade for low SNR as shown for the first simulation (**Fig. 2A**, last row plot).

Therefore, a clear observation is that the curse of overfitting increases for low SNR. In these cases, knowing the actual generative model could not ensure robust estimators as overfitting can occur either when estimating the state or space equation or balanced in between. For example, estimating a model with a high degree of freedom (DOF) for the estimator  $\hat{\mathbf{x}}_t$  and a low DOF for the estimator  $\hat{\mathbf{A}}_p$  (e.g., a sparse estimator of the autoregressive coefficients) could be as harmful as estimating a model with a low DOF for  $\hat{\mathbf{x}}_t$  (e.g., a sparse spatiotemporal solution) and a high DOF for  $\hat{\mathbf{A}}_p$ , despite good data fitting. Therefore, a pertinent question is how do we select the correct model with actual data in large-scale analysis? A sensible answer is to use data-driven regularization based on  $K$ -fold cross-validation, as the next section demonstrates.

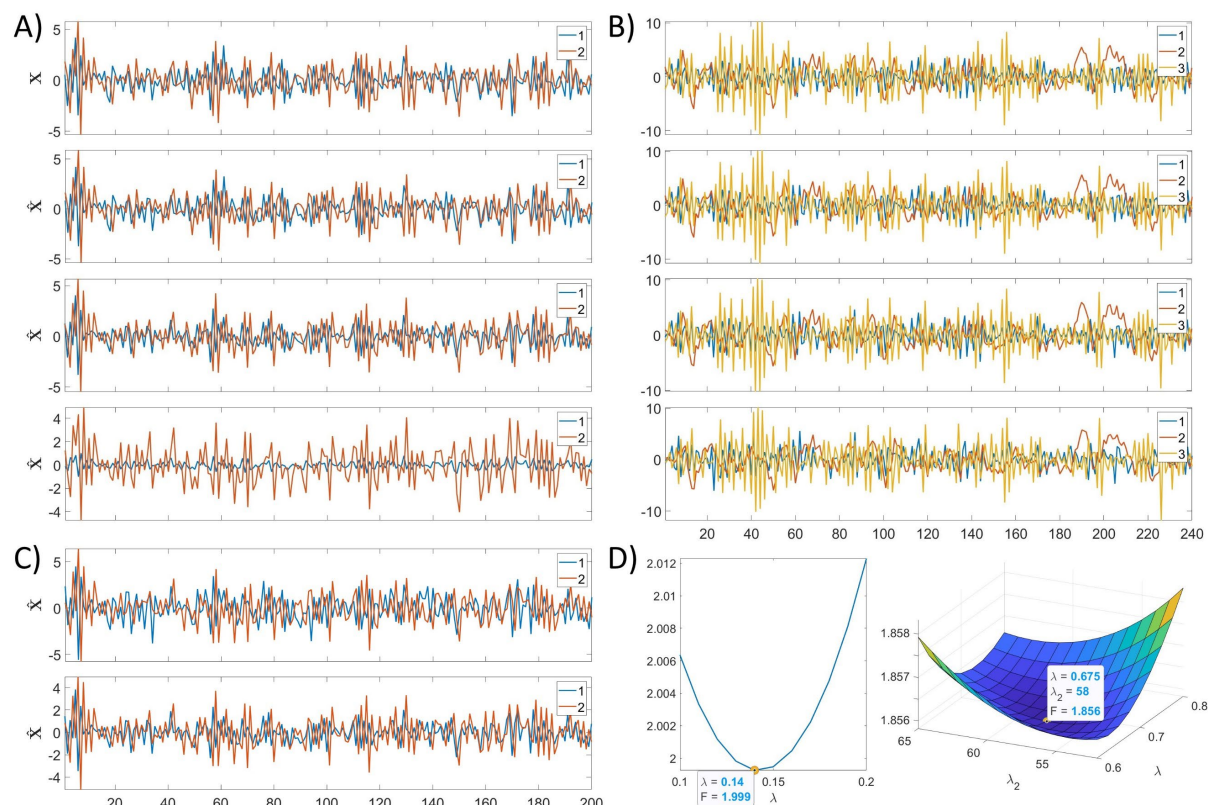


**Figure 2:** Original and estimated dynamics ( $\mathbf{x}$  and  $\hat{\mathbf{x}}$ ) for the state-space model using the SSGD algorithm, which corresponds to the estimated autoregressive coefficients shown in **Tables 1 and 2** for the simulations with lag=1 (**A**), and lag=1,2,3 (**B**). From top to bottom are plotted the ground-truth dynamics generated with **Eqs. (1, 2)** and the estimated solutions for the different observation noise levels  $\sigma_o = 0.1$ ,  $\sigma_o = 0.5$ , and  $\sigma_o = 1$  in this order. Correspondingly for each simulation, the two- or three-variate time series plots are highlighted with different colors for a clear visual comparison of the estimators versus the ground-truth values. (**C**) Two more solutions were estimated for the lag=1 simulation by solving MPSS models as stated in **Eqs. (3, 4)**, using  $K = 5$  fold cross-validation based on imputed data ( $K$ -fold CV) to select the hyperparameters. Whereas for the first regularized solution (top row), only  $\lambda$  was adjusted in the model (line search), for the second regularized solution (bottom row) both  $\lambda$  and  $\lambda_2^{(a)}$  are assessed (plane search). The other hyperparameters are set to zero. (**D**) Corresponding to the line and plane search, the cross-validation predicted error (**Eq. (16)** in **Online Methods**) curves are shown, together with the selected hyperparameter values and minimum value of cost function.

## Hyperparameter estimation using $K$ -fold cross-validation based on imputed data

Here, we proposed an extension of classical  $K$ -fold cross-validation to deal with the estimation of regularization parameters in MPSS models (**Online Methods**) and demonstrated that it could help to control overfitting. We used the SSGD algorithm to explore different regularization parameter combinations, firstly, for the bivariate time-series simulation in the noisiest scenario (**Figs. 2C, D**), and secondly, for the three-variate simulation in the noisier scenarios (**Fig. 3**).

For the first analysis, **Fig. 2A** (bottom row) showed the estimated dynamics for the naïve estimator in the worst SNR case, with RSE of 0.752 and 0.326 (reproduced for clarity; see also corresponding solution  $\hat{\mathbf{A}}_p$  in **Table 1**). It is clear that overfitting affected the solutions. Initially, we search only for a more appropriate value of  $\lambda$  than its naïve value, i.e., setting the other hyperparameters to zero. Thus, this is the case of a single hyperparameter search or line search. Then, we searched only for more appropriate values for hyperparameters  $\lambda$  and  $\lambda_2^{(a)}$ , corresponding to the case of a grid or plane search. We used  $K = 5$  folds in our cross-validation procedure to implement the search in both cases, and SSGD used  $\alpha = 1$  and momentum  $\mu = 0.99$ . We found that the best-predicted error for the line-search case is  $F \approx 1.999$ , achieved for  $\lambda = 0.14$  (**Fig. 2D**, left plot), with RSE statistics of 0.653 and 0.261 corresponding to the solution  $\hat{\mathbf{x}}_t$  (**Fig. 2C**, top row). Whereas, for the plane search, the cross-validation's predicted error improves to  $F \approx 1.856$ , achieved for  $\lambda \approx 0.675$  and  $\lambda_2^{(a)} = 58$  (**Fig. 2D**, right plot), with RSE statistics of 0.314 and 0.179 for  $\hat{\mathbf{x}}_t$  (**Fig. 2C**, bottom row). **Extended Data Table 3** shows the outcome for the estimated autoregressive coefficients in these analyses.

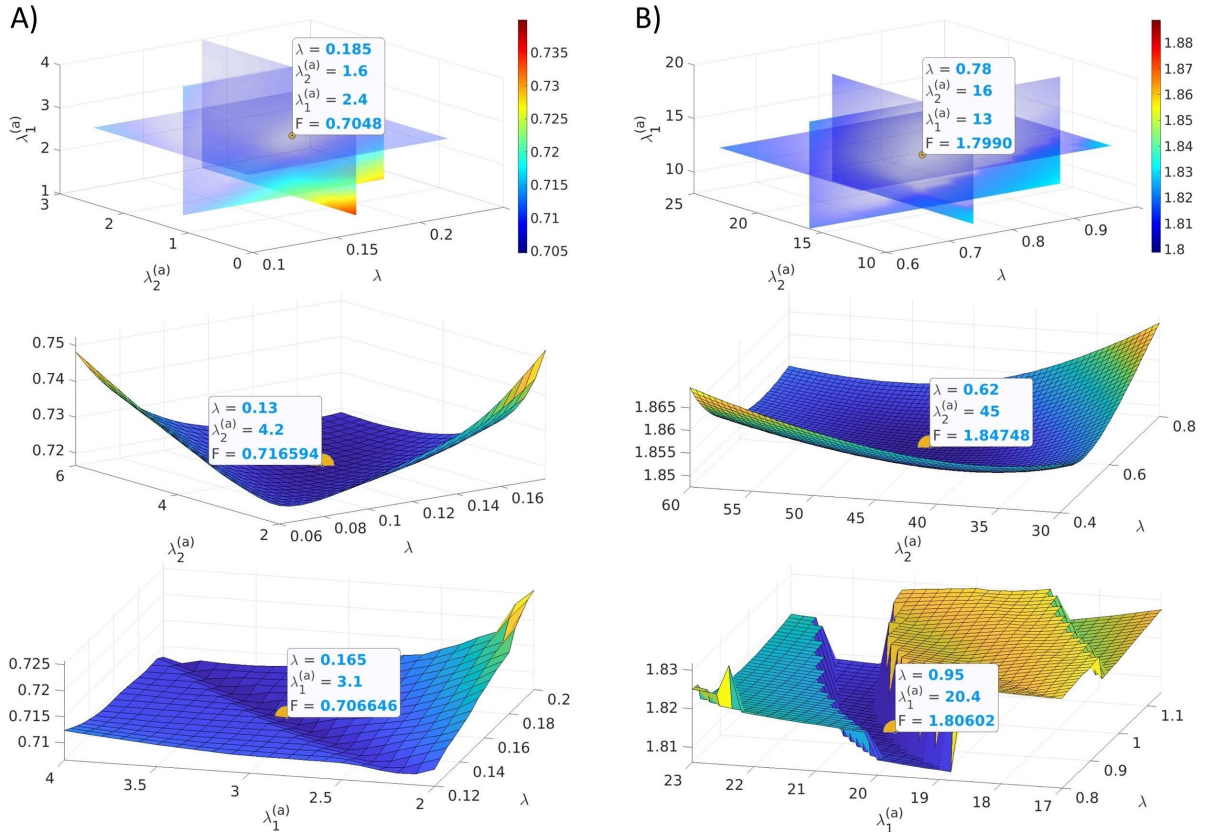


**Figure 3:**  $K$ -fold cross-validation based on imputed data ( $K$ -fold CVI; see **Online Methods**). Here, it is demonstrated for the three-variate lag=1,2,3 simulation, for the noisier scenarios (A)  $\sigma_o = 0.5$  and (B)  $\sigma_o = 1$ . The subplots show the prediction error (Eq. (16) in **Online Methods**) curves, evaluated for the separated multigrid search analyses corresponding to the subspaces  $\{(\lambda, \lambda_2^{(a)}, \lambda_1^{(a)}) \mid \lambda \geq 0, \lambda_2^{(a)} \geq 0, \lambda_1^{(a)} \geq 0\}$ ,  $\{(\lambda, \lambda_2^{(a)}) \mid \lambda \geq 0, \lambda_2^{(a)} \geq 0\}$ , and  $\{(\lambda, \lambda_1^{(a)}) \mid \lambda \geq 0, \lambda_1^{(a)} \geq 0\}$  as shown from top to bottom in this order.



For the second analysis, in contrast, we ran two- and three-dimensional subspaces search for the lower SNR simulations and plotted the corresponding prediction error curves (**Fig. 3**). For clarity, for the naïve estimator, the values of the RSE statistic are 0.067, 0.042, and 0.018, for  $\sigma_o = 0.5$  (3,671,869 iterations,  $\alpha = 10^{-2}$ ), and 0.327, 0.183, and 0.075 for  $\sigma_o = 1$  (18,715,396 iterations,  $\alpha = 10^{-3}$ ). In comparison, for the regularized solutions, for the same replica in the  $\sigma_o = 0.5$  scenario, the RSE statistics are 0.052, 0.037, and 0.015 (7,532 iterations), 0.055, 0.038, and 0.016 (7,912 iterations), and 0.054, 0.037, and 0.015 (7,559 iterations), for the solutions corresponding to the search over subspaces  $(\lambda, \lambda_2^{(a)}, \lambda_1^{(a)})$ ,  $(\lambda, \lambda_2^{(a)})$ , and  $(\lambda, \lambda_1^{(a)})$ , in this order. While, for the same replica in the  $\sigma_o = 1$  scenario, the statistics are 0.118, 0.100, and 0.038 (6,440 iterations), 0.120, 0.099, and 0.038 (8,200 iterations), and 0.116, 0.098, and 0.037 (9,164 iterations), correspondingly. We used  $\alpha = 1$  and momentum  $\mu = 0.99$  in the regularization analysis. These results revealed the advantages of fitting MPSS models with the proposed data-driven regularization approach. **Extended Data Table 4** shows the estimated autoregressive coefficients for each regularization analysis.

Summarizing, our observations are, firstly, regularization has a noticeable positive effect on the estimation of better models, with the best solutions achieved when more regularization parameters were considered. Additionally, using the  $\ell_1$ -norm-based regularization produced sparse estimators as expected (**Extended Data Table 4**). Secondly, despite the increased computational time due to the hyperparameter search, regularization improves the numerical condition for optimization problems<sup>46</sup>, adding stability to the solutions, which can be appreciated as SSGD converged remarkably faster for regularized than for naïve estimators. However, searching the hyperparameter subspaces should be exercised with caution because the values can change abruptly, as shown by the ridged valley in **Fig. 3B** (bottom row), and can also change dramatically with the SNR level and the number of hyperparameters.

Finally, to compare against the state-of-the-art, we also calculated the solutions for these two simulations using the standard and Bayesian implementation for state-space models<sup>47</sup>, available in Matlab R2022a's Econometric toolbox: functions "ssm.estimate" and "bssm.estimate". For the standard implementation, we used constrained (Matlab "fmincon" function) and interior-point search optimization as other settings failed to produce acceptable solutions (check code settings in **Extended Data Tables 7-12**). These settings are not needed with the Bayesian solver as it assumes a *priori* Gaussian distributions for the parameters, initial state variables and observation errors, which covariances can be estimated using Monte Carlo simulations or importance sampling methods<sup>47</sup>. Interestingly, in all cases, our regularized approach based on the SSGD algorithm produced better results than state-of-the-art, particularly for lowest SNR simulations. This superiority was more evident for the more complex scenarios. For example, for the three-variate lag=1,2,3 simulation for  $\sigma_o = 1$ , compare the outcomes in **Extended Data Table 4**, second half, against the standard and Bayesian solutions shown in **Extended Data Table 6**. Regarding the computational time for this analysis, the longest duration of a regularized approach run, including the 5-fold plane search and the calculation of the final regularized solution, was about 27 and 48 seconds for the  $\sigma_o = 0.5$  and  $\sigma_o = 1$  cases, with grid-search dimensions of 6x9 and 11x21 tested hyperparameter values, respectively. In comparison, the Matlab's standard and Bayesian solutions took about 59 and 115, and 157 and 323 seconds, respectively, as shown in the outcome of **Extended Data Table 6**. However, this is only a rough comparison as the time in our analysis depends on the number of  $K$  folds, the grain resolution of searching subspaces and the number of hyperparameters, and we also do not take into account the coding differences among these algorithms. Finally, an unquestionable advantage of our methods is that they produce both  $\hat{\mathbf{x}}_t$  and  $\hat{\mathbf{A}}_p$  estimates while state-of-the-art methods often produce only estimators for  $\hat{\mathbf{A}}_p$ , the initial state variables and observation errors.

## Alternating least square (ALS) and HGDALS algorithms to solve the MPSS model

Despite the promise of the SSGD, it is necessary to investigate more efficient methods for large-scale analysis. Fortunately, our optimization problem is quadratic, and solving the optimization problem separately for  $\{x_t\}$ ,  $t = 1, \dots, T$ , and  $\{A_p\}$ ,  $p = 1, \dots, P$ , produces closed-form solutions (Eq. (17, 20) in **Online Methods**). This estimation of  $x_t$  and  $A_p$  results in a novel alternating least squares (ALS) algorithm to solve state-space models. To illustrate the simplicity of this idea, Fig. 4 shows its application to a toy example.

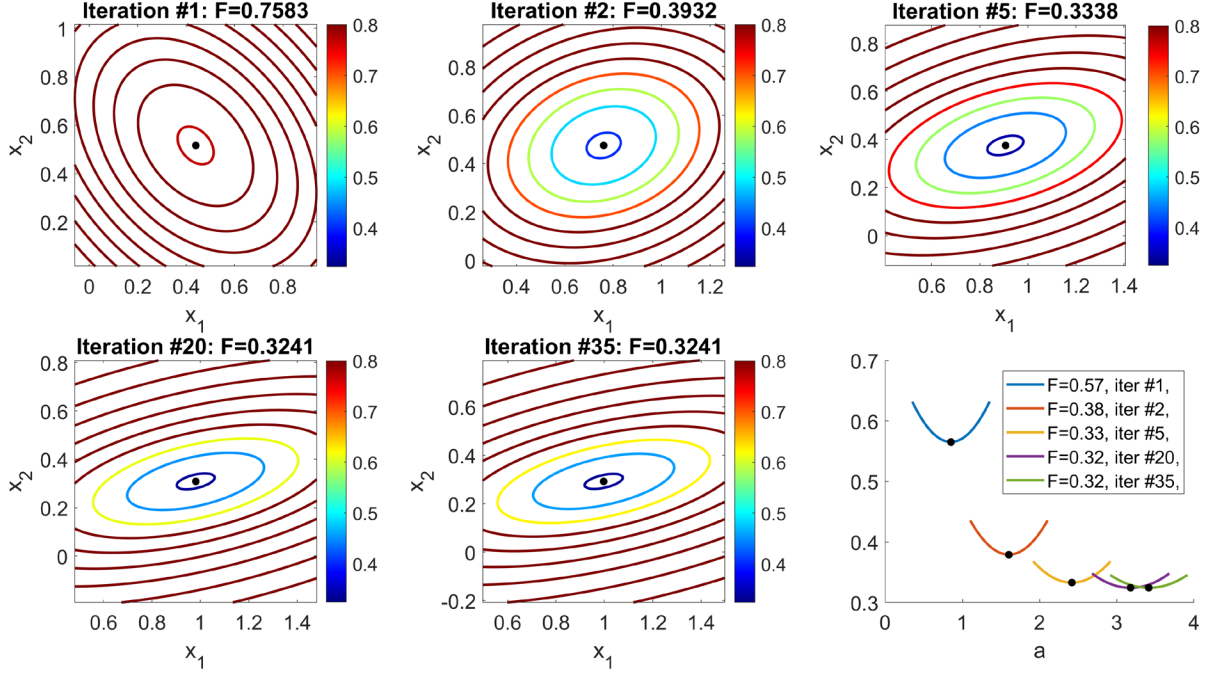


**Figure 4:** Convergence of the alternating least squares (ALS) algorithm for a toy example. The optimization (cost) function is  $\left\| \begin{pmatrix} 1 \\ 1 \end{pmatrix} - \begin{pmatrix} 1 & 0.5 \\ 0.3 & 0.8 \end{pmatrix} \begin{pmatrix} x_1 \\ x_2 \end{pmatrix} \right\|_2^2 + (x_1 - ax_2)^2 + x_2^2$ , equivalent to  $\left\| \begin{pmatrix} 1 \\ 1 \end{pmatrix} - \begin{pmatrix} 1 & 0.5 \\ 0.3 & 0.8 \end{pmatrix} \begin{pmatrix} x_1 \\ x_2 \end{pmatrix} \right\|_2^2 + \left\| \begin{pmatrix} 1 & -a \\ 0 & 1 \end{pmatrix} \begin{pmatrix} x_1 \\ x_2 \end{pmatrix} \right\|_2^2$ , which is evaluated for the particular solutions as shown for selected iterations (contours and curves) in subplots. We compute

$$x(k+1) = \left( \begin{pmatrix} 1 & 0.5 \\ 0.3 & 0.8 \end{pmatrix}^T \begin{pmatrix} 1 & 0.5 \\ 0.3 & 0.8 \end{pmatrix} + \begin{pmatrix} 1 & -a(k) \\ 0 & 1 \end{pmatrix}^T \begin{pmatrix} 1 & -a(k) \\ 0 & 1 \end{pmatrix} \right)^{-1} \begin{pmatrix} 1 & 0.5 \\ 0.3 & 0.8 \end{pmatrix}^T \begin{pmatrix} 1 \\ 1 \end{pmatrix},$$

from an initial value  $a(0)$ , and subsequently calculate  $a(k+1) = -x_1(k+1)/x_2(k+1)$ , iteratively. The subplots also show the optimal iterative solution (centred marked point) and its cost function value in the title or legend. In this example, the ALS algorithm converged after 35 iterations as the iterative solution's cost function cannot be further reduced, as illustrated by interweaving the values shown in the title of subplots (row-major order) with the ones in the legend of last subplot. In the first five subplots, the colormaps highlight the changes in curvature of the cost function for  $x$  across the iterations. In the last subplot, the colors highlight the cost function curves for different iterations. As can be seen, interleaving the cost function values at the iterative solutions from both calculation steps above forms a strictly monotonic decreasing sequence that converges to a fixed point, as expected from the ALS algorithm<sup>48</sup>.

More general than the ALS algorithm, we propose HGDALS – a hybrid method between GD and ALS (**Extended Data Table 2** and **Online Methods**). HGDALS interleaves GD and ALS calculations by applying one step of ALS with as many steps of GD ( $I_{GD}$ ) as calculated by the formula

$$\frac{\Delta F_{GD}}{\Delta F_{ALS}} \approx \frac{I_{GD} T_{GD}}{T_{ALS}},$$

which balances the ratio between the optimization function changes by GD ( $\Delta F_{GD}$ ) and ALS ( $\Delta F_{ALS}$ ) with the ratio of their computational time ( $T_{GD}$  and  $T_{ALS}$ ) for the previous iteration. Thus, producing an approximate integer value for the number of iterations  $I_{GD}$ . HGDALS is a flexible algorithm because if ALS is not producing dramatically faster local convergence than GD, then HGDALS increases the number of GD iterations.

## Solving large-scale MPSS models for synthetic MEG data

We test ALS/HGDALS with a large-scale simulation based on a MEG/EEG toolbox in Matlab<sup>49</sup>. The toolbox contains data for an individual brain, including high- and low-resolution cortical surface meshes with 74,382 and 2,004 vertices, respectively. The high-resolution mesh allows us to overlay the cortical surface results, while the low-resolution mesh vertices provide the locations for dipoles in our analysis. The toolbox also provides leadfield matrices calculated for MEG and EEG forward problems, assuming that dipoles are perpendicularly oriented to the cortical surface, and using 298 and 108 sensors, respectively. We simulate only MEG data; therefore,  $M = 298$  and  $N = 2004$ .

In the simulations, we set the sampling frequency  $F_s = 250$  Hz and  $P = 5$  (lag=1,...,5). We also set  $T = 30$  due to the high dimensionality of the matrices in the algorithmic implementation (e.g., calculations involve the left-division by a sparse matrix of dimensions  $NT \times NT$ ). However, we compensate for the small number of samples by generating  $E = 200$  epochs. Thus, our simulation corresponds more closely to an event-related experiment, with signals recorded from multiple trials in controlled conditions. Notice that we use the same MVAR matrices to generate  $\mathbf{x}_t^{(e)}$ ,  $e = 1, \dots, E$ , randomly and independently for each epoch for  $SNR = 20$  decibels. Finally, after the generation, the matrices  $\mathbf{x}_t^{(e)}$  and  $\mathbf{A}_p$  become the ground truth for the analysis (see **Online Methods** for additional information, including the autoregressive matrices for lag=1,...,5).

**Fig. 5** shows several outcomes from this analysis. The HGDALS solution at the time instant  $t = 28$  reveals the estimated source activity that approximately matches the simulated sources at the left-hemisphere occipital, inferior temporal, and bilateral (symmetric) somatosensory cortices (**Fig. 5A**, top row). In comparison, using the minimum norm inverse solution (**Fig. 5A**, bottom row), which is approximately equivalent to the HGDALS solution for a single iteration, it is unclear where the relevant brain activity takes place with so many salient spots in the solution. For a less experimented analyst, it could be confusing to analyze these solutions because of the high- and low-intensity patches that lie adjacent to each other. An expert can realize that some of these patches with opposed polarity could correspond to the same underlying source, as estimated dipoles with opposite polarities tend to lie on the opposite walls surrounding a brain sulcus. Thus, they will have similar waveforms but opposite signs (see **Extended Data Fig. 1**).

To better identify the source locations, from the total amount of  $N = 2004$  dipoles, we selected the 100 more salient dipoles according to the average spectral energy (**Extended Data Fig. 2**). As shown in **Fig. 5B**, using four views of the cortical surface, we corroborated that these dipoles are in clusters around the five simulated ground-truth sources (see also **Extended Data Fig. 3**). Additionally, **Fig. 5C** shows that the estimated time-series dynamics for these dipoles are also very close to the ground-truth simulated epoched waveforms for each of the corresponding ground-truth sources, after manually correcting for the polarity sign (**Extended Data Figure 1**). As expected, the time-series estimation is more accurate for the posterior than anterior regions, with the anterior/posterior description according to the network precedence in the simulated connectivity map (**Fig. 5F**).

Finally, **Figs. 5D, E** show the ground truth and estimated connectivity matrices for the five sources and the most salient 100 dipoles, respectively, which also revealed outstanding results despite the higher dimension. For example, notice the very accurate recovery of the inhibitory and excitatory interregional connectivity patches, particularly for the selected dipoles that correspond to the simulated regions actively communicating for lag=2,3,4 in the ground-truth maps. Namely, source 1  $\rightarrow$  3 (excitatory) for lag 2, 1  $\rightarrow$  3 (inhibitory) and 1  $\rightarrow$  4 (excitatory) for lag 3, and 1  $\rightarrow$  4 (inhibitory) for lag 4. Finally, notice that the estimated interactions in the block diagonals for lag=1,2 (i.e., intraregional communication among the salient dipoles in a cluster around the same ground-truth

simulated source) are mostly excitatory for lag=1 and inhibitory for lag=2, which agrees with the ground truth for each lagged interaction.

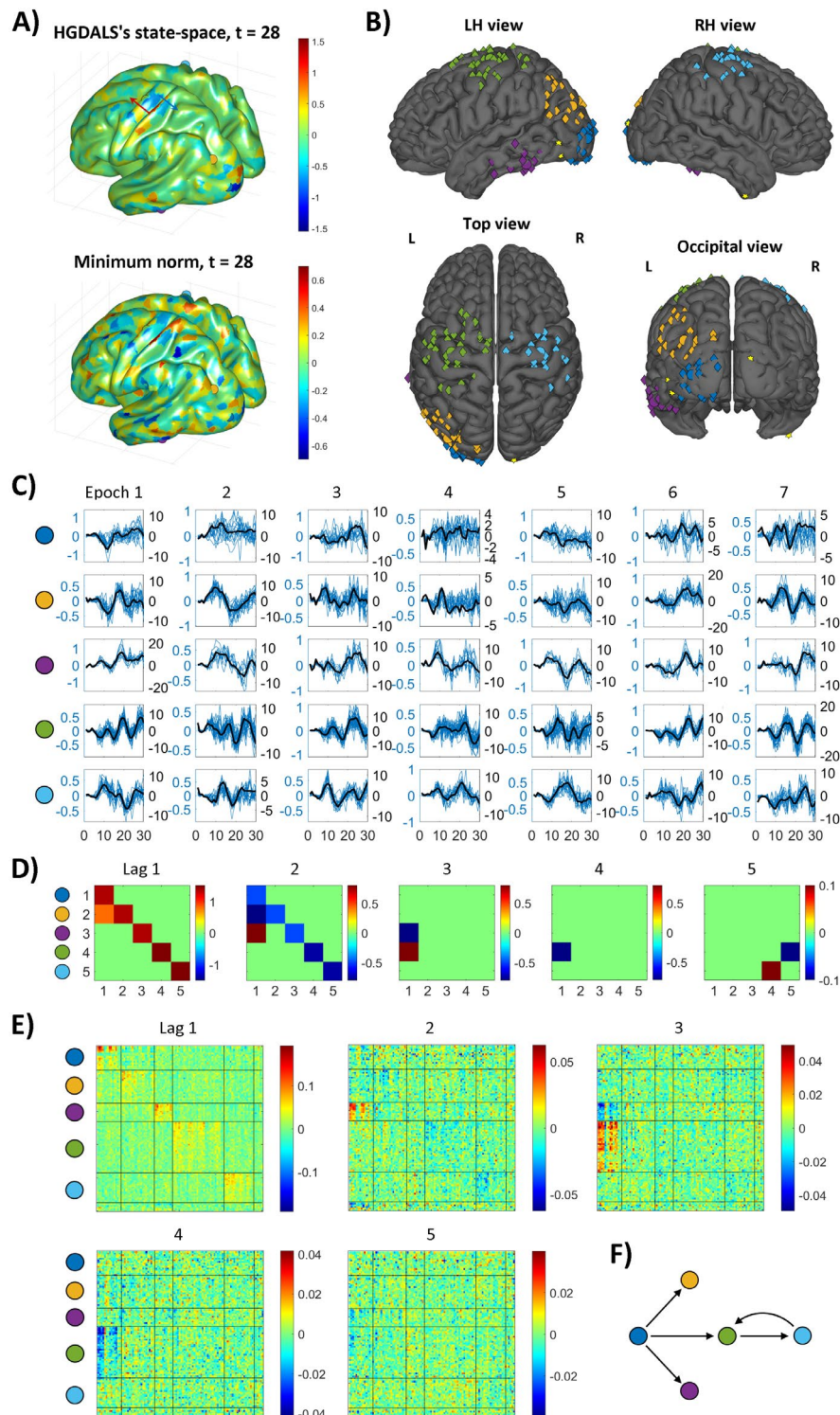


**Figure 5:** Large-scale simulation based on simulated MEG data. (A) HGDALS's (top) and minimum norm (bottom) solutions at instant  $t = 28$ . Colormaps highlight the signal intensity. (B) Four views of the cortical locations of the most salient 100 estimated dipoles (colored diamonds and yellow stars for correct and false recovery, respectively), together with ground-truth sources (colored circles). Different colors for each source (C) Estimated temporal dynamics correspond to 96 of 100 correctly estimated dipoles (blue curves), together with corresponding ground-truth source time-series (black curves), separately for each source (rows) and selected epochs (columns). (D) Connectivity map for ground truth, dimension is  $5 \times 5$  for each lag=1,...,5. (E) Estimated connectivity maps for the 100 selected dipoles, grouped by clusters according to the corresponding sources in the order as indicated by colored circles. The horizontal and vertical lines highlight the clusters. (F) Graph of ground-truth connections highlighting the flow of information (i.e., ignoring the delay).

## Solving large-scale MPSS models for actual event-related MEG/EEG data

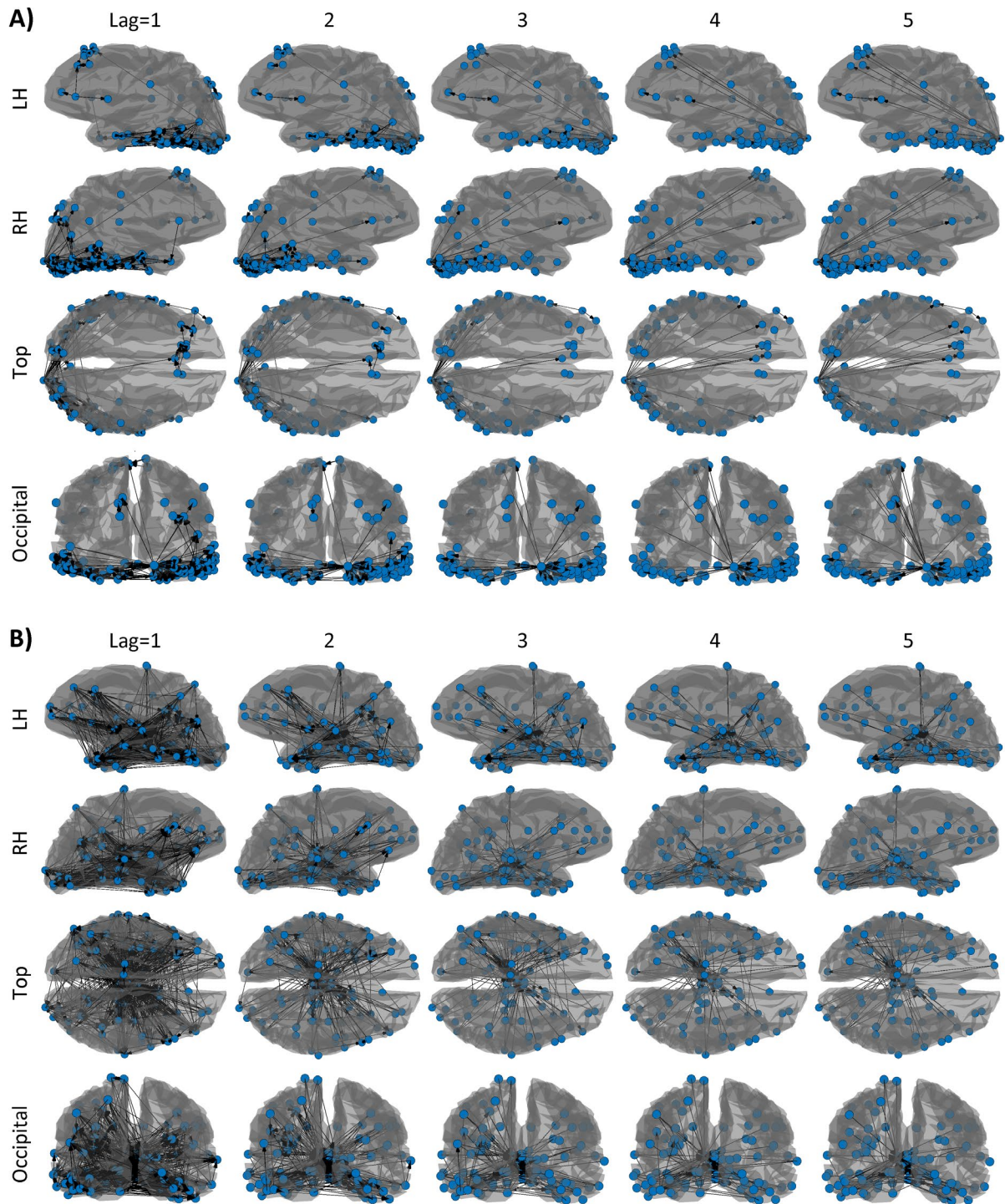
The MEG/EEG data analyzed in this section corresponds to a single subject from the Wakeman and Henson study<sup>50</sup>. We are only interested in a proof-of-concept due to the substantial computational cost of this large-scale analysis. The study also compiled individual anatomical MRI images and cortical surface segmentation. We used Fieldtrip<sup>51</sup> to calculate the MEG/EEG leadfields with dipoles perpendicularly oriented to the cortical surface and used the scripts provided by the study to run preprocessing analysis, particularly for the familiar faces stimulus<sup>50</sup>. After controlling for eye-movements artifacts, we extracted the same 203 epochs for MEG and EEG analyses. All signals were filtered using a Butterworth low-pass filter for 25 Hz and downsampled to 250 Hz. In the analysis, we used  $F_S = 250$  Hz and  $P = 5$ ,  $\text{lag}=1,\dots,5$ , to estimate the past influences. As introduced in the section above, we solved the MPSS modified optimization problem for epoched data. Due to the computational cost of the algorithm, instead of calculating the entire time-varying FC, we conducted the analysis only for the time window of [100, 200] milliseconds posterior to the stimulus onset, according to the latency of face processing<sup>52</sup> and because it showed significant activity for this dataset (Wakeman and Henson's Fig. 1a<sup>50</sup>).

Figure **6A** shows the results for analysis involving the EEG signals, which reveal an interesting flow of information from the occipital to the inferior temporal lobe. This process corresponds to activation of the ventral stream of the visual cortex<sup>52-54</sup>, which is also a notable finding because of the consistency of flow direction. Although in a lower amount, there is also communication with parietal and frontal regions, with the information critically flowing from the visual cortex to these areas. The other exciting and consistent finding is that the interacting regions are mainly close to each other for the minor lags ( $\text{lag}=1,2$ , equivalent to influences from 4 to 8 milliseconds in the past). In contrast, the number of long-range interactions increases for the higher lags ( $\text{lag}=4,5$ , influences from 16 to 20 milliseconds in the past), particularly between the occipital and frontal regions.

On the other hand, **Figure 6B** reveals a contradictory observation for the MEG-based results. In this case, using only the MEG signals (from both magnetometer and gradiometer channels), we can capture subcortical structures that create a hub of incoming information mainly from visual and temporal areas. This finding is also tenable as the processing of face information involves subcortical brain areas such as the amygdala and hippocampus, as evidenced in studies using MEG/EEG<sup>55,56</sup> and concurrent intracortical recordings<sup>56</sup>.

## Discussion

We have proposed a data-driven regularization approach to solve large-scale state-space models, simultaneously solving the brain source localization and functional connectivity problems. With clear distinction from previous research<sup>3-9</sup>, we have solved this problem directly in the natural high-dimensional manifold of brain activations and functional connectivity (FC), i.e., without reducing dimensions as in previous works<sup>4,8,10</sup>. The classical methods to solve state-space models are based on Kalman filter and expectation maximization<sup>3-10</sup>, which have issues to deal with massive data or more complex scenarios as empirically demonstrated here. However, we show that straightforward algorithms such as backpropagation (see **Fig. 1** and **Extended Data Table 1**) could find the solutions even with moderate noisy data. As revealed by training ANNs, backpropagation allows us to solve high-dimensional problems<sup>57</sup>, and it is the most favored algorithm<sup>42</sup>, which served here as inspiration to develop related but more suitable algorithms to solve state-space models in large-scale analysis.



**Figure 6:** Estimated functional connectivity maps using the HGDALS algorithm for MPSS models. The estimated connections are projected in the individual brain cortical surface separately for each lagged interaction (lag=1,...,5, along the rows), with each connectivity map shown from different orientations (along the columns). **(A)** Analysis conducted using EEG data. **(B)** Analysis conducted using MEG data.

By discussing state-space models in large dimensions, we exposed the critical negative impact of overfitting in model estimation, widely overlooked in this field<sup>3-10</sup>. With the introduction of multiple penalized state-space (MPSS) models, we demonstrated that using a data-driven regularization approach, based on a novel extension of  $K$ -fold cross-validation, can control overfitting. To solve the MPSS models, we proposed a state-space gradient descent (SSGD) algorithm, which can inherit most of the tricks used to train ANNs with backpropagation, as both algorithms share the same iterative

approach based on GD optimization. For example, we showed that SSGD could use momentum modification, and future implementations could incorporate stochastic GD, mini-batch GD, and other tricks<sup>42</sup>. Interestingly, SSGD performed much better than backpropagation in our simulation analyses by converging faster (using larger  $\alpha$  step sizes) and being more robust when using momentum. These results support two interesting future investigations: 1) SSGD could render better results than backpropagation to train ANNs, and 2) MPSS models can provide a framework to test backpropagation, SSGD, and other alternative ANNs algorithms in more realistic scenarios, as long as the unicity of the solution is guaranteed. The MPSS framework enables testing with different SNR levels and could allow the implementation of designed adversarial attacks<sup>58</sup>.

We finally introduced an alternative least squares (ALS) algorithm and its hybrid combination with SSGD (HGDALS). It enabled us to solve MPSS models with thousands of variables in the hidden state and its corresponding connectivity matrices. Remarkably, the ALS algorithm provides iteratively closed-form expressions that helped us to clearly state that the brain source localization and FC problems complement and constraint each other (**Fig. 4** and **Online Methods**). This finding exposes a critical failure of other statistical methods in the literature that have ignored this dependency<sup>22–25</sup>.

Notice that our extension of the classical  $K$ -fold cross-validation approach for state-space models (**Fig. 1E** and **Online Methods**) is critical to implementing the MPSS framework. Our case is similar to time series forecasting, where there is no straightforward application for the cross-validation technique due to temporally correlated signals<sup>59</sup>. However, we provided a solution based on a practical data imputation procedure that is possible given the MPSS framework (**Eqs. (14, 15)** in **Online Methods**). Other cross-validation implementations, including nested cross-validation, could be evaluated in future analysis. However, notice that these variants may assume unrealistically that noise is uncorrelated<sup>59</sup> or increase the computational time without significant advantages<sup>60</sup>.

To our knowledge, this is the first time that such high-dimensional analysis has been effectively conducted for state-space models using a data-driven regularization approach while harnessing the power of high-performance computing (HPC). Particularly, we used a V100-PCIe GPU device with 32 GB RAM and 7 (14) teraflops for double- (single-) precision calculations, available at the Northern Ireland's HPC (NI-HPC) cluster, to ensemble the large but sparse matrices required for the ALS/HGDALS algorithms. However, we conducted the division step using Matlab's function `mldivide`, which performs left-side matrix division multicore very efficiently for sparse matrices. In our case, for 30 CPU cores, Matlab's sparse division was significantly faster than using NVIDIA's `cuSPARSE` and `cuSOLVER` libraries. However, this could change in the future as NVIDIA libraries improve and because, after a recent upgrade, the NI-HPC now provides modern A100-SXM GPU devices with 80 GB RAM and 19.5 teraflops for both double- and single-precision calculations. Furthermore, our ALS/HGDALS implementation could also be made more efficient. For example, it could be applied iteratively with variable selection<sup>61</sup>, or sparse regularization as shown here for the SSGD algorithm, or using Group-LASSO regularization as demonstrated by a related approach<sup>25</sup>.

Ultimately, our goal is to solve simultaneously two challenging open problems of MEG/EEG neuroimaging – namely, the brain source localization and FC problems. The ALS algorithm is a very well-suited solver as it relies on a quadratic optimization problem (**Eqs. 22, 23** in **Online Methods**) that encompasses on one side the linearity of the source localization problem, which is due to the electromagnetic quasi-static assumptions<sup>62</sup>, and on the other side the linear predictive expression of MVAR models, widely used to solve the FC problem<sup>11,20</sup>. For the latter, a possible criticism is that neural mass<sup>3,63</sup> or spiking neuronal modeling<sup>64</sup> may better represent the nonlinear nature of neuronal dynamics. How it may affect the accuracy of solutions, or whether modification of

backpropagation, SSGD and ALS/HGDALS algorithms can consider nonlinear generative models, are attractive ideas that deserve further research.

Moreover, it might be interesting to speculate about what to expect if either ALS/HGDALS or any other algorithm becomes a proper Oracle method for MEG/EEG signals — as with the MRI algorithm for MRI/fMRI signals, which provides accurate pictures of in-vivo brains using radio frequency pulses and acquired spin echo signals. Then, it would be valid to ask what we should expect if this Oracle uses only MEG or EEG data? We hypothesize that the independently estimated brain sources must have similar spatiotemporal patterns, and the estimated MEG- and EEG-based FC networks must be very similar. This hypothesis was tested here by applying ALS/HGDALS to actual MEG/EEG data<sup>50</sup> (**Fig. 6**). For EEG data, the results revealed activation of the ventral stream of the visual system with information flow from occipital to inferior-temporal regions. In contrast, MEG results revealed activity hubs in subcortical regions. These results, including the significant occipitotemporal activations in both analyses, are consistent with the literature<sup>53–56</sup>.

However, the differences between MEG/EEG outcomes are noticeable. We can attribute these differences to several factors. Firstly, ALS/HGDALS may be far from an Oracle method. Secondly, MEG and EEG signals have different sensitivity for the perpendicular/tangential orientation of a source or its depth<sup>65</sup>. Thirdly, the impact of miss-specifications of the head models used in MEG/EEG forward problems to estimate the respective leadfield matrices may significantly affect FC estimation<sup>66</sup>. Lastly, the simple reality of EEG sensors attached to the scalp, whereas the MEG sensors have no fixed reference, may have a significant impact. Thus, we consider that MEG signals may be affected in non-trivial ways due to head (and thereby brain sources) movement during a recording session.

Finally, we conducted a single-subject analysis of MEG/EEG data due to the still expensive computational cost, about three days on a single V100 GPU device with 30 CPU cores. This cost does not seem dramatic, but the total time can be significant when considering multiple subjects and the possibility of conducting dynamic FC analysis based on the sliding time-window technique<sup>67</sup>. As we improve the MPSS framework, we will perform these analyses in future studies for all the subjects in the database<sup>50</sup> and study the dynamic FC changes.

## Online content

Any methods, extended data figures and tables, and statements of code availability are accessible in the paper's online version.

## Acknowledgments

The authors are grateful for access to the Tier 2 High-Performance Computing resources provided by the Northern Ireland High Performance Computing (NI-HPC) facility funded by the UK Engineering and Physical Sciences Research Council (EPSRC), Grant No. EP/T022175/1. RCS was partially supported by grant RGPIN-2022-03042 from the Natural Sciences and Engineering Research Council of Canada.

## References

1. *Niedermeyer's electroencephalography : basic principles, clinical applications, and related fields*. (OUP USA, 2018).
2. Raichle, M. E. The Brain's Default Mode Network. *Annu. Rev. Neurosci.* **38**, 433–447 (2015).



3. Friston, K. J., Harrison, L. & Penny, W. Dynamic causal modelling. *Neuroimage* **19**, 1273–1302 (2003).
4. Cheung, B. L. P., Riedner, B. A., Tononi, G. & Van Veen, B. D. Estimation of Cortical Connectivity From EEG Using State-Space Models. *IEEE Trans. Biomed. Eng.* **57**, 2122–2134 (2010).
5. Shumway, R. H. & Stoffer, D. S. AN APPROACH TO TIME SERIES SMOOTHING AND FORECASTING USING THE EM ALGORITHM. *J. Time Ser. Anal.* **3**, 253–264 (1982).
6. Van de Steen, F. *et al.* Critical Comments on EEG Sensor Space Dynamical Connectivity Analysis. *Brain Topogr.* **32**, 643–654 (2019).
7. Yamashita, O., Galka, A., Ozaki, T., Biscay, R. & Valdes-Sosa, P. Recursive Penalized Least Squares Solution for Dynamical Inverse Problems of EEG Generation. *Hum. Brain Mapp.* **21**, 221–235 (2004).
8. Galka, A., Yamashita, O., Ozaki, T., Biscay, R. & Valdés-Sosa, P. A solution to the dynamical inverse problem of EEG generation using spatiotemporal Kalman filtering. *Neuroimage* **23**, 435–453 (2004).
9. Barton, M. J. *et al.* Evaluating the performance of Kalman-filter-based EEG source localization. *IEEE Trans. Biomed. Eng.* **56**, 122–136 (2009).
10. Long, C. J. *et al.* State-space solutions to the dynamic magnetoencephalography inverse problem using high performance computing. *Ann. Appl. Stat.* **5**, 1207–1228 (2011).
11. Bastos, A. M. & Schoffelen, J.-M. A Tutorial Review of Functional Connectivity Analysis Methods and Their Interpretational Pitfalls. *Front. Syst. Neurosci.* **9**, 1–23 (2016).
12. Pascual-Marqui, R. D. R. D. Review of methods for solving the EEG inverse problem. *Int. J. Bioelectromagn.* **1**, 75–86 (1999).
13. Pascual-Marqui, R. D., Michel, C. M. & Lehmann, D. Low resolution electromagnetic tomography: a new method for localizing electrical activity in the brain. *Int. J. Psychophysiol.* **18**, 49–65 (1994).
14. Sekihara, K. & Nagarajan, S. S. Minimum-Norm-Based Source Imaging Algorithms. in *Electromagnetic Brain Imaging* vol. 30 9–28 (Springer International Publishing, 2015).
15. Sekihara, K., Nagarajan, S. S., Poeppel, D., Marantz, A. & Miyashita, Y. Reconstructing spatio-temporal activities of neural sources using an MEG vector beamformer technique. *IEEE Trans. Biomed. Eng.* **48**, 760–771 (2001).
16. Gross, J. *et al.* Dynamic imaging of coherent sources: Studying neural interactions in the human brain. *Proc. Natl. Acad. Sci.* **98**, 694–699 (2001).
17. Vega-Hernández, M., Martínez-Montes, E., Sánchez-Bornot, J. M., Lage-Castellanos, A. & Valdés-Sosa, P. A. Penalized Least Squares methods for solving the EEG Inverse Problem. *Stat. Sin.* **18**, 1535–1551 (2008).
18. Van Veen, B., van Drongelen, W., Yuchtman, M. & Suzuki, A. Localization of brain electrical activity via linearly constrained minimum variance spatial filtering. *IEEE Trans. Biomed. Eng.* **44**, 867–880 (1997).
19. Buckner, R. L., Krienen, F. M. & Yeo, B. T. T. Opportunities and limitations of intrinsic functional connectivity MRI. *Nat. Neurosci.* **16**, 832–837 (2013).

20. Valdes-Sosa, P. A. *et al.* Granger Causality on Spatial Manifolds: Applications to Neuroimaging. in *Handbook of Time Series Analysis* 461–491 (Wiley-VCH Verlag GmbH & Co. KGaA, 2006). doi:10.1002/9783527609970.ch18.
21. Nolte, G. *et al.* Identifying true brain interaction from EEG data using the imaginary part of coherency. *Clin. Neurophysiol.* **115**, 2292–2307 (2004).
22. Mahjoory, K. *et al.* Consistency of EEG source localization and connectivity estimates. *Neuroimage* **152**, 590–601 (2017).
23. Hincapié, A. S. *et al.* The impact of MEG source reconstruction method on source-space connectivity estimation: A comparison between minimum-norm solution and beamforming. *Neuroimage* **156**, 29–42 (2017).
24. Pirondini, E. *et al.* Computationally efficient algorithms for sparse, dynamic solutions to the EEG source localization problem. *IEEE Trans. Biomed. Eng.* **65**, 1359–1372 (2018).
25. Manomaisaowapak, P., Nartkulpat, A. & Songsiri, J. Granger Causality Inference in EEG Source Connectivity Analysis: A State-Space Approach. *IEEE Trans. Neural Networks Learn. Syst.* 1–11 (2021) doi:10.1109/TNNLS.2021.3096642.
26. Sanchez-Bornot, J. M., Wong-Lin, K. F., Ahmad, A. L. & Prasad, G. Robust EEG/MEG Based Functional Connectivity with the Envelope of the Imaginary Coherence: Sensor Space Analysis. *Brain Topogr.* **0**, 1–22 (2018).
27. Cao, J. *et al.* Brain functional and effective connectivity based on electroencephalography recordings: A review. *Hum. Brain Mapp.* **43**, 860–879 (2022).
28. Power, J. D., Barnes, K. A., Snyder, A. Z., Schlaggar, B. L. & Petersen, S. E. Spurious but systematic correlations in functional connectivity MRI networks arise from subject motion. *Neuroimage* **59**, 2142–2154 (2012).
29. Greicius, M. D., Supekar, K., Menon, V. & Dougherty, R. F. Resting-state functional connectivity reflects structural connectivity in the default mode network. *Cereb. Cortex* **19**, 72–78 (2009).
30. Frässle, S. *et al.* Regression dynamic causal modeling for resting-state fMRI. *Hum. Brain Mapp.* **42**, 2159–2180 (2021).
31. Brookes, M. J. *et al.* Measuring functional connectivity using MEG: Methodology and comparison with fcMRI. *Neuroimage* **56**, 1082–1104 (2011).
32. Tewarie, P. *et al.* Tracking dynamic brain networks using high temporal resolution MEG measures of functional connectivity. *Neuroimage* **200**, 38–50 (2019).
33. Sanchez-Bornot, J. M. *et al.* High-dimensional brain-wide functional connectivity mapping in magnetoencephalography. *J. Neurosci. Methods* **348**, (2021).
34. Hillebrand, A., Barnes, G. R., Bosboom, J. L., Berendse, H. W. & Stam, C. J. Frequency-dependent functional connectivity within resting-state networks: An atlas-based MEG beamformer solution. *Neuroimage* **59**, 3909–3921 (2012).
35. Raghupathi, W. & Raghupathi, V. Big data analytics in healthcare: promise and potential. *Heal. Inf. Sci. Syst.* **2**, 1–10 (2014).
36. Werbos, P. J. Backpropagation Through Time: What It Does and How to Do It. *Proc. IEEE* **78**, 1550–1560 (1990).

37. Rumelhart, D. E., Hinton, G. E. & Williams, R. J. Learning representations by back-propagating errors. *Nature* **323**, 533–536 (1986).
38. Silver, D. *et al.* Mastering the game of Go with deep neural networks and tree search. *Nature* **529**, 484–489 (2016).
39. Liao, R. *et al.* Reviving and improving recurrent back-propagation. *35th Int. Conf. Mach. Learn. ICML 2018* **7**, 4807–4820 (2018).
40. Lillicrap, T. P., Santoro, A., Marris, L., Akerman, C. J. & Hinton, G. Backpropagation and the brain. *Nat. Rev. Neurosci.* **21**, 335–346 (2020).
41. Lillicrap, T. P. & Santoro, A. Backpropagation through time and the brain. *Curr. Opin. Neurobiol.* **55**, 82–89 (2019).
42. Yang, G. R. & Wang, X. J. Artificial Neural Networks for Neuroscientists: A Primer. *Neuron* **107**, 1048–1070 (2020).
43. Chen, H., Lu, F. & He, B. Topographic property of backpropagation artificial neural network: From human functional connectivity network to artificial neural network. *Neurocomputing* **418**, 200–210 (2020).
44. Grech, R. *et al.* Review on solving the inverse problem in EEG source analysis. *J. Neuroeng. Rehabil.* **5**, 1–33 (2008).
45. Stokes, P. A. & Purdon, P. L. Correction: A study of problems encountered in Granger causality analysis from a neuroscience perspective (Proc Natl Acad Sci USA (2018) 114 (E7063–E7072) DOI: 10.1073/pnas.1704663114). *Proc. Natl. Acad. Sci. U. S. A.* **115**, E6964 (2018).
46. Tikhonov, A. N. & Arsenin, V. I. A. *Solutions of ill-posed problems*. (John Wiley & Sons Inc, 1977).
47. James Durbin & Koopman, S. J. *Time Series Analysis by State Space Methods*. (OUP Oxford, 2012).
48. Langville, A. N., Meyer, C. D., Albright, R., Cox, J. & Duling, D. Algorithms, Initializations, and Convergence for the Nonnegative Matrix Factorization. (2014).
49. Haufe, S. & Ewald, A. A Simulation Framework for Benchmarking EEG-Based Brain Connectivity Estimation Methodologies. *Brain Topogr.* 1–18 (2016) doi:10.1007/s10548-016-0498-y.
50. Wakeman, D. G. & Henson, R. N. A multi-subject, multi-modal human neuroimaging dataset. *Sci. data* **2**, 150001 (2015).
51. Oostenveld, R., Fries, P., Maris, E. & Schoffelen, J. M. FieldTrip: Open source software for advanced analysis of MEG, EEG, and invasive electrophysiological data. *Comput. Intell. Neurosci.* **2011**, (2011).
52. Lin, J. F. L., Silva-Pereyra, J., Chou, C. C. & Lin, F. H. The sequence of cortical activity inferred by response latency variability in the human ventral pathway of face processing. *Sci. Rep.* **8**, 1–11 (2018).
53. Miller, K. J., Hermes, D., Pestilli, F., Wig, G. S. & Ojemann, J. G. Face percept formation in human ventral temporal cortex. *J. Neurophysiol.* **118**, 2614–2627 (2017).
54. Goodale, M. A. & Milner, A. D. Separate visual pathways for perception and action. *Trends*

- Neurosci.* **15**, 20–25 (1992).
55. Dumas, T. *et al.* MEG Evidence for Dynamic Amygdala Modulations by Gaze and Facial Emotions. *PLoS One* **8**, 1–11 (2013).
  56. Dubarry, A. S. *et al.* Simultaneous recording of MEG, EEG and intracerebral EEG during visual stimulation: From feasibility to single-trial analysis. *Neuroimage* **99**, 548–558 (2014).
  57. Bengio, Y. Deep learning of representations: Looking forward. *Lect. Notes Comput. Sci. (including Subser. Lect. Notes Artif. Intell. Lect. Notes Bioinformatics)* **7978 LNAI**, 1–37 (2013).
  58. Akhtar, N. & Mian, A. Threat of Adversarial Attacks on Deep Learning in Computer Vision: A Survey. *IEEE Access* **6**, 14410–14430 (2018).
  59. Bergmeir, C., Hyndman, R. J. & Koo, B. A note on the validity of cross-validation for evaluating autoregressive time series prediction. *Comput. Stat. Data Anal.* **120**, 70–83 (2018).
  60. Wainer, J. & Cawley, G. Nested cross-validation when selecting classifiers is overzealous for most practical applications. *Expert Syst. Appl.* **182**, 115222 (2021).
  61. Hastie, T., Friedman, J. & Tibshirani, R. *The Elements of Statistical Learning*. (Springer New York, 2001). doi:10.1007/978-0-387-21606-5.
  62. Nolte, G. The magnetic lead field theorem in the quasi-static approximation and its use for magnetoencephalography forward calculation in realistic volume conductors. *Phys. Med. Biol.* **48**, 3637–3652 (2003).
  63. Sotero, R. C., Trujillo-Barreto, N. J., Iturria-Medina, Y., Carbonell, F. & Jimenez, J. C. Realistically Coupled Neural Mass Models Can Generate EEG Rhythms. *Neural Comput.* **19**, 478–512 (2007).
  64. Gerstner, W., Lehmann, M., Liakoni, V., Corneil, D. & Brea, J. Eligibility Traces and Plasticity on Behavioral Time Scales: Experimental Support of NeoHebbian Three-Factor Learning Rules. *Front. Neural Circuits* **12**, 1–16 (2018).
  65. Ahlfors, S. P., Han, J., Belliveau, J. W. & Hämäläinen, M. S. Sensitivity of MEG and EEG to source orientation. *Brain Topogr.* **23**, 227–232 (2010).
  66. Cho, J. H., Vorwerk, J., Wolters, C. H. & Knösche, T. R. Influence of the head model on EEG and MEG source connectivity analyses. *Neuroimage* **110**, 60–77 (2015).
  67. Hindriks, R. *et al.* Can sliding-window correlations reveal dynamic functional connectivity in resting-state fMRI? *Neuroimage* **127**, 242–256 (2016).
  68. Barnett, L. & Seth, A. K. The MVGC multivariate Granger causality toolbox: A new approach to Granger-causal inference. *J. Neurosci. Methods* **223**, 50–68 (2014).
  69. Ringo, J. L., Doty, R. W., Demeter, S. & Simard, P. Y. Time Is of the Essence: A Conjecture that Hemispheric Specialization Arises from Interhemispheric Conduction Delay. *Cereb. Cortex* **4**, 331–343 (1994).

## Online Methods

### Backpropagation algorithm for state-space models

We show the graphical representation of algebraic operations in **Fig. 1** for the state-space model in **Eqs. 1, 2** (shown in the main text), together with a practical application for simultaneously solving the brain source localization and functional connectivity (FC) problems. The model is stated for the general case when it considers one or more delayed influences, and its graph resembles the unrolled graph of interactions in recurrent neural networks (RNNs)<sup>36,41</sup>, where the autoregressive weights  $\mathbf{A}_p$ ,  $p = 1, \dots, P$ , play a similar role to the shared weights in an RNN. **Extended Data Table 1** shows the backpropagation implementation to solve this state-space model.

**Extended Data Table 1:** Backpropagation algorithm for the state-space model represented in **Eqs. (1, 2)** and **Fig. 1B**.

| <b>Error function</b>   |
|---|
| $F = \frac{1}{2T} \sum_{t=1}^T (\mathbf{z}_t - \mathbf{y}_t)^2,$ <p>where <math>\mathbf{z}_t</math> and <math>\mathbf{y}_t</math> represent the measured data and predicted outcome, respectively, from the backpropagation forward pass step.</p>  |
| <b>Forward propagation (for <math>i = 1, \dots, I</math> iterations)</b>  |
| $\mathbf{x}_t(i) = \mathbf{v}_t(i); \text{ for } t = 1, \dots, P,$ $\mathbf{x}_t(i) = \sum_{p=1}^P \mathbf{A}_p(i) \mathbf{x}_{t-p}(i) + \mathbf{v}_t(i); \text{ for } t = P + 1, \dots, T,$ $\mathbf{y}_t(i) = \mathbf{B} \mathbf{x}_t(i); \text{ for } t = 1, \dots, T.$  |
| <b>Partial derivatives using chain rule for the <math>i</math>-th iteration (iteration index removed for simplicity)</b>  |
| $\delta_t^y = \partial F / \partial \mathbf{y}_t = -(\mathbf{z}_t - \mathbf{y}_t) / T; \text{ for } t = 1, \dots, T,$ $\delta_T^x = \partial F / \partial \mathbf{x}_T = \mathbf{B}^T \delta_T^y,$ $\delta_t^x = \partial F / \partial \mathbf{x}_t = \mathbf{B}^T \delta_t^y + \sum_{p=\max(P+1-t, 1)}^{\min(P, T-t)} \mathbf{A}_p^T \delta_{t+p}^x; \text{ calculate backwards for } t = T - 1, \dots, 2, 1.$ <p>Note that application of the chain rule is backwards for proper calculations/updates. Also note that, although dynamics in <math>\mathbf{x}_t</math> affect <math>\mathbf{x}_{t+1}, \dots, \mathbf{x}_{t+p}</math>, in the extreme cases <math>\mathbf{x}_{T-1}</math> only affects <math>\mathbf{x}_T</math>, and <math>\mathbf{x}_1</math> only affects <math>\mathbf{x}_{P+1}</math>, in agreement with the forward propagation rule (previous step).</p>   |
| <b>Parameters update using gradient descent</b>   |
| $\mathbf{v}_t(i+1) = \mathbf{v}_t(i) - \alpha (\delta_t^x + (\lambda/T) \mathbf{v}_t(i)); \text{ for } t = 1, \dots, T,$ $\mathbf{A}_p(i+1) = \mathbf{A}_p(i) - \alpha \sum_{t=P+1}^T \delta_t^x \mathbf{x}_{t-p}(i)^T; \text{ for } p = 1, \dots, P,$ <p>where <math>\alpha</math> is the step size adopted along the gradient descent direction. Here, <math>\lambda \geq 0</math> is a regularization parameter often used to implement weight decay in the training of ANNs, which can be justified using a Bayesian interpretation and assuming that the noise terms <math>\mathbf{v}_t</math> follow a normal distribution. Similarly, we can rewrite the second expression as <math>\mathbf{A}_p(i+1) = \mathbf{A}_p(i) - \alpha (\sum_{t=P+1}^T \delta_t^x \mathbf{x}_{t-p}(i)^T + (\lambda_2/T) \mathbf{A}_p(i))</math>, with <math>\lambda_2 \geq 0</math>; however, for simplicity, we ignored in our research the application of weight decay on the estimation of <math>\mathbf{A}_p</math>, for <math>p = 1, \dots, P</math>.</p> |

In the implementation of the backpropagation algorithm, the state equation's error terms  $\mathbf{v}_t$ ,  $t = 1, \dots, T$ , are directly estimated, which allows obtaining the hidden (internal) state dynamics with the generative expression:

$$\mathbf{x}_t(i) = \sum_{p=1}^P \mathbf{A}_p(i) \mathbf{x}_{t-p}(i) + \mathbf{v}_t(i); \text{ for } t = P + 1, \dots, T.$$

Also, notice that we are penalizing the error term, bringing us to a regularized optimization problem (instead of the original optimization function shown in the table):

$$F = \frac{1}{2T} \sum_{t=1}^T \{(\mathbf{z}_t - \mathbf{y}_t)^2 + \lambda \|\mathbf{v}_t\|_2^2\},$$

which is similar to the expression in Ridge regression<sup>61</sup>, known as weight decay in the training of ANNs.

### State-space gradient descent algorithm based on a Bayesian interpretation of the backpropagation framework

Here, we examine state-space models from a Bayesian perspective by considering conditional and *a priori* probability distributions. In our particular case, we consider the following assumptions:

- The conditional distribution for the observation variable:

$$\mathbf{y}_t | \mathbf{B}, \mathbf{x}_t \sim N(\mathbf{B}\mathbf{x}_t, \sigma_o^2 \mathbf{I}_M). \quad (5)$$

- The conditional distribution for the state variable:

$$\mathbf{x}_{t>P} | \{\mathbf{A}_1, \dots, \mathbf{A}_P\}, \{\mathbf{x}_1, \dots, \mathbf{x}_{t-1}\} \sim N(\sum_{p=1}^P \mathbf{A}_p \mathbf{x}_{t-p}, \sigma_s^2 \mathbf{I}_N). \quad (6)$$

- The a priori distribution for the state variable:

$$\mathbf{x}_{t \leq P} \sim N(\mathbf{0}_N, \sigma_s^2 \mathbf{I}_N), \quad (7)$$

where  $\mathbf{0}_N$  and  $\mathbf{I}_N$  are the zero vector and the identity matrix with  $N$  elements and  $N \times N$  dimension, respectively.

- The a priori distribution for the autoregressive coefficients:

$$\text{vec}(\mathbf{A}) \sim N(\mathbf{0}_{N^2P}, \sigma_{2,a}^2 \mathbf{I}_{N^2P}), \quad (8)$$

where  $\mathbf{A} = [\mathbf{A}_1, \dots, \mathbf{A}_P] \in \mathcal{R}^{N \times NP}$  is the matrix that contains all the autoregressive coefficients, shown by using Matlab notation for horizontal concatenation for a better understanding, and  $\text{vec}(\mathbf{A})$  is the vectorized representation, which follows from Matlab column-major notation.

- Additionally, we can also use sparse priors:

$$\text{vec}(\mathbf{x}) \sim \text{Laplace}(\mathbf{0}, \sigma_{1,x}^2 \mathbf{I}_{NT}), \quad (9)$$

where  $\mathbf{x}$  contains all the state's variables for all time instants, similar to the notation used for  $\mathbf{A}$ , and/or

$$\text{vec}(\mathbf{A}) \sim \text{Laplace}(\mathbf{0}, \sigma_{1,a}^2 \mathbf{I}_{N^2P}). \quad (10)$$

Although, in practice, we may only adopt the *a priori* assumptions, as in **Eqs. (8-10)**, in a large-scale scenario. In general, using a Bayesian framework allows us to propose multiple penalized state-space (MPSS) models. From this formulation, computing the maximum a posteriori estimate for the parameters  $\mathbf{x} \in \mathbb{R}^{N \times T}$  and  $\mathbf{A} \in \mathcal{R}^{N \times NP}$  is equivalent to solving the MPSS optimization problem shown in **Eqs. (3, 4)** (see the main text).

As alternative to the backpropagation technique introduced above, we propose a state-space gradient descent (SSGD) technique for solving the MPSS models represented. SSGD is implemented based on the following partial derivatives:

$$T \frac{\partial F}{\partial \mathbf{x}_t} = \begin{aligned} & -\mathbf{B}^T(\mathbf{y}_t - \mathbf{B}\mathbf{x}_t) + \lambda(\mathbf{x}_t - \sum_{p=1}^P \mathbf{A}_p \mathbf{x}_{t-p}) \\ & - \lambda \sum_{q=1}^{\min(P, T-t)} \mathbf{A}_q^T (\mathbf{x}_{t+q} - \sum_{p=1}^P \mathbf{A}_p \mathbf{x}_{t+q-p}) + \lambda_1^{(x)} \text{sgn}(\mathbf{x}_t); \end{aligned} \quad (11)$$

for  $t = P + 1, \dots, T$ .

$$T \frac{\partial F}{\partial \mathbf{x}_t} = \begin{aligned} & -\mathbf{B}^T(\mathbf{y}_t - \mathbf{B}\mathbf{x}_t) - \lambda \sum_{q=\max(P+1-t, 1)}^{\min(P, T-t)} \mathbf{A}_q^T (\mathbf{x}_{t+q} - \sum_{p=1}^P \mathbf{A}_p \mathbf{x}_{t+q-p}); \\ & + \lambda \mathbf{x}_t + \lambda_1^{(x)} \text{sgn}(\mathbf{x}_t); \end{aligned} \quad (12)$$

for  $t = 1, \dots, P$ .

$$T \frac{\partial F}{\partial \mathbf{A}_p} = -\lambda \sum_{t=P+1}^T (\mathbf{x}_t - \sum_{q=1}^P \mathbf{A}_q \mathbf{x}_{t-q}) \mathbf{x}_{t-p}^T + \lambda_1^{(a)} \text{sgn}(\mathbf{A}) + \lambda_2^{(a)} \mathbf{A}; \quad (13)$$

for  $p = 1, \dots, P$ .

### **K-fold cross-validation based on imputed data for state-space models**

We propose an extension of the original  $K$ -fold cross-validation method<sup>61</sup> to estimate the prediction error in state-space models as represented in **Eqs. (1, 2)**. As in the original cross-validation method, we randomly separate the data samples (time points' measurements in our case) into  $K$ -fold subsets. One critical difference, in our case, the data corresponds to the temporal sequence  $\mathbf{y}_t$ ,  $t = 1, \dots, T$ , with an underlying autoregressive (generative) model. Because leaving out a patch of adjacent samples is highly detrimental to the model estimation due to the temporal dependency. Thus, we implement the  $K$ -fold partition by dividing the samples into nonoverlapping adjacent time windows of length  $K$  and subsequently randomly assigning each time-window sample to one of the  $K$ -fold subsets. This procedure guarantees a balanced partition of the samples into  $K$  subsets  $\{y_{\tau_1}^{(1)}, \dots, y_{\tau_{|S_1|}}^{(1)}\} \in S_1, \dots, \{y_{\tau_1}^{(K)}, \dots, y_{\tau_{|S_K|}}^{(K)}\} \in S_K$ , where  $|S|$  represents the subset's cardinality. At the same time, it guarantees that no more than two adjacent time-instant samples are assigned to the same subset (see **Fig. 1E** for the case of  $K = 5$  and  $T = 200$ ).

The other essential difference with the classical cross-validation approach is that usually, the data consists of pairs  $(\mathbf{x}_t, \mathbf{y}_t)$ , which are assigned randomly to each  $K$ -fold subset. However, in our state-space model, we only know  $\mathbf{y}_t$  and  $\mathbf{x}_t$  must be estimated together with the other model parameters. Therefore, for each  $K$ -fold run, to estimate the prediction error for the hold-out samples  $\{\mathbf{y}_\tau\} \in S_k$ , we first have to estimate their corresponding "missing" part  $\{\mathbf{x}_\tau\}$ . Reflecting on this feature, we refer to our procedure as  $K$ -fold cross-validation based on imputed data ( $K$ -fold CVI) as we need first to impute  $\{\mathbf{x}_\tau\}$  by treating  $\{\mathbf{y}_\tau\} \in S_k$  as missing values, for each run  $k = 1, \dots, K$ , before evaluating the prediction error.

Corresponding to this modification, we change the MPSS optimization function to account for the  $K$ -fold hold-out subset at each  $K$ -fold iteration, as follows:

$$F_k = \frac{1}{2T} \left\{ \sum_{t=1}^T L_t^{(k)} \|\mathbf{y}_t - \mathbf{B}\mathbf{x}_t\|_2^2 + \lambda \sum_{t=P+1}^T \|\mathbf{x}_t - \sum_{p=1}^P \mathbf{A}_p \mathbf{x}_{t-p}\|_2^2 \right\} \\ + \lambda \sum_{t=1}^P \|\mathbf{x}_t\|_2^2 + \lambda_2^{(a)} \|\mathbf{A}\|_F^2 + 2\lambda_1^{(x)} \|\mathbf{x}\|_1 + 2\lambda_1^{(a)} \|\mathbf{A}\|_1 \quad (14)$$

for  $k = 1, \dots, K$ ,

$$\hat{\mathbf{x}}^{(k)}, \hat{\mathbf{A}}^{(k)} = \underset{\mathbf{x}, \mathbf{A}}{\text{argmin}} F_k(\mathbf{x}, \mathbf{y}, \mathbf{A}, \mathbf{B}, \lambda, \lambda_2^{(a)}, \lambda_1^{(x)}, \lambda_1^{(a)}), \quad (15)$$

where  $L_t^{(k)} = \begin{cases} 0, & \text{if } y_t \in S_k \\ 1, & \text{otherwise} \end{cases}$  is a cost function, set up to remove the contribution of the hold-out data samples  $\{\mathbf{y}_\tau\} \in S_k$  for each  $K$ -fold run.

After that, we calculate the prediction error, averaging the errors for the predicted observation for each hold-out sample, for all the  $K$ -fold runs:





in the quadratic case, as ALS alone produces very fast convergence to the solution. However, combining GD and ALS complementary features could render better results for a general nonlinear optimization problem. HGDALS relies on applying one iteration of ALS with as many iterations,  $I_{GD}$ , of GD as calculated by the formula

$$\frac{\Delta F_{GD}}{\Delta F_{ALS}} = \frac{I_{GD}T_{GD}}{T_{ALS}}, \quad (21)$$

which balances the ratio between the optimization function changes by GD ( $\Delta F_{GD}$ ) and ALS ( $\Delta F_{ALS}$ ) with the ratio of their computational time for a single (previous) iteration. Therefore, if ALS is not producing faster local convergence than GD, HGDALS will automatically increase the number of GD's iterations. Conveniently, we simultaneously limit the number of GD's iterations, so the GD's total time is not more than, for example, the 20% of ALS computational time, i.e.,  $I_{GD}T_{GD} \leq 0.2T_{ALS}$ . A summary of the HGDALS follows in **Extended Data Table 2**.

**Extended Data Table 2:** HGDALS algorithm.

```

 $I_{GD} = 1;$ 
for  $i = 1, \dots, I$ 
   $F = \text{function\_evaluation}();$ 
   $\text{time} = \text{clock}();$ 
  <model optimization with ALS>
   $T_{ALS} = \text{clock}() - \text{time};$ 
   $\Delta F_{ALS} = F - \text{function\_evaluation}();$ 

  if ( $i > 1$ )
     $I_{GD} = \min(0.2 T_{ALS}/T_{GD}, \text{ceil}((\Delta F_{GD}T_{ALS})/(\Delta F_{ALS}T_{GD})));$ 
  end

   $F = \text{function\_evaluation}();$ 
   $\text{time} = \text{clock}();$ 
  for  $j = 1, \dots, I_{GD}$ 
    <model optimization with GD>
  end
   $T_{GD} = (\text{clock}() - \text{time})/I_{GD};$ 
   $\Delta F_{GD} = F - \text{function\_evaluation}();$ 
end

```

### Large-scale analysis and algorithms modification for epoched data to speed computations

Finally, we discuss a large-scale simulation based on Haufe and Ewald's MEG/EEG toolbox in Matlab<sup>49</sup>. This toolbox provides high- and low-resolution mesh data (surface's triangles and vertices points) for the called New York brain, with 74,382 and 2,004 vertices, respectively. The high-resolution mesh allows plotting the results in the brain cortical surface. At the same time, the low-resolution vertices provide the locations to calculate the dynamic state variables in our procedure; therefore,  $N = 2004$ . The toolbox also provides leadfield matrices calculated for MEG and EEG forward problems for dipoles perpendicularly oriented to the cortical surface. In our case,  $M = 298$  as we simulated only MEG data. As the dimension of the matrices in **Eq. (17)** is  $NT \times NT$ , then we could not use a value of  $T > 50$ , even though we used V100 GPU cards with 32 GB RAM and a multicore (30 cores) computer, so we fixed  $T = 30$  in our simulations. Additionally, we set the sampling frequency  $F_S = 250$  Hz (equivalent to 4 milliseconds time resolution) and  $P = 5$  (lag=1,...,5), which is equivalent to considering influences as long as 20 milliseconds from the past.

To be as realistic as possible, we should set  $P$  accordingly to neurophysiological data, with the evidence pointing to communication delays as long as 40-50 milliseconds<sup>69</sup>. However, due to

numerical instability, using larger P values makes it challenging to tune these simulations for appropriate values of the autoregressive coefficients  $\mathbf{A}_p$ . In these simulations, we use these coefficients matrices (presented from the left to right inside brackets) for lag=1,...,5:

$$\mathbf{A} = \left\{ \left( \begin{array}{ccccc} 1.356 & 0 & 0 & 0 & 0 \\ 0.8 & 1.356 & 0 & 0 & 0 \\ 0 & 0 & 1.356 & 0 & 0 \\ 0 & 0 & 0 & 1.5 & 0 \\ 0 & 0 & 0 & 0 & 1.5 \end{array} \right), \left( \begin{array}{ccccc} -0.49 & 0 & 0 & 0 & 0 \\ -0.8 & -0.49 & 0 & 0 & 0 \\ 0.8 & 0 & -0.49 & 0 & 0 \\ 0 & 0 & 0 & -0.75 & 0 \\ 0 & 0 & 0 & 0 & -0.75 \end{array} \right), \right. \\ \left. \left( \begin{array}{ccccc} 0 & 0 & 0 & 0 & 0 \\ 0 & 0 & 0 & 0 & 0 \\ -0.8 & 0 & 0 & 0 & 0 \\ 0.8 & 0 & 0 & 0 & 0 \\ 0 & 0 & 0 & 0 & 0 \end{array} \right), \left( \begin{array}{ccccc} 0 & 0 & 0 & 0 & 0 \\ 0 & 0 & 0 & 0 & 0 \\ 0 & 0 & 0 & 0 & 0 \\ -0.8 & 0 & 0 & 0 & 0 \\ 0 & 0 & 0 & 0 & 0 \end{array} \right), \left( \begin{array}{ccccc} 0 & 0 & 0 & 0 & 0 \\ 0 & 0 & 0 & 0 & 0 \\ 0 & 0 & 0 & 0 & 0 \\ 0 & 0 & 0 & 0 & -0.1 \\ 0 & 0 & 0 & 0.1 & 0 \end{array} \right) \right\}$$

Notice that we plotted the connectivity maps corresponding to these values in **Fig. 5D**, and the simplified (without delays) directed graph in **Fig. 5F**.

On the other hand, using  $T = 30$  could be considered a substantial limitation concerning the vast number of parameters. Fortunately, there is a trick that we can exploit to run our calculations with a much larger number of samples. As usual in event-related studies, many trials or epochs are recorded for the same stimulation paradigm and under the same conditions. Therefore, we adapt to this situation by running many replications (epochs) of our simulation with the fixed MVAR coefficients above. Corresponding to this modification, we have to adapt the MPSS optimization function for the multiple epochs case as follows:

$$F_k = \frac{1}{2TE} \left\{ \begin{array}{l} \sum_{e=1}^E \sum_{t=1}^T L_t^{(k)} \left\| \mathbf{y}_t^{(e)} - \mathbf{B}\mathbf{x}_t^{(e)} \right\|_2^2 \\ + \lambda \sum_{e=1}^E \sum_{t=p+1}^T \left\| \mathbf{x}_t^{(e)} - \sum_{p=1}^P \mathbf{A}_p \mathbf{x}_{t-p}^{(e)} \right\|_2^2 \\ + \lambda \sum_{e=1}^E \sum_{t=1}^P \left\| \mathbf{x}_t \right\|_2^2 + \lambda_2^{(x)} \left\| \mathbf{X} \right\|_F^2 + \lambda_2^{(a)} \left\| \mathbf{A} \right\|_F^2 \end{array} \right\}, \quad (22)$$

for  $k = 1, \dots, K$ ,

$$\hat{\mathbf{x}}^{(k)}, \hat{\mathbf{A}}^{(k)} = \underset{\mathbf{x}, \mathbf{A}}{\operatorname{argmin}} F_k(\mathbf{x}, \mathbf{y}, \mathbf{A}, \mathbf{B}, \lambda, \lambda_2^{(x)}, \lambda_2^{(a)}), \quad (23)$$

where  $E$  is the number of epochs. In this case, we state our optimization problem based only on the hyperparameters  $\lambda, \lambda_2^{(x)}$ , and  $\lambda_2^{(a)}$ . We ignored the use of sparse penalty functions (corresponding to using  $\lambda_1^{(a)}$  or  $\lambda_1^{(x)}$ ) due to the higher computational cost. Notice that although we fix the MVAR matrices for every epoch, the generated time-series  $\mathbf{x}_t^{(e)}$ ,  $e = 1, \dots, E$ , change randomly and independently across the epochs. We set  $E = 200$  in the simulations.

Interestingly, this last optimization problem can be solved very efficiently as long as we run the  $K$ -fold partition only for the time dimension, i.e., a unique partition of the temporal indices for all the epochs (coded by the loss function  $L_t^{(k)}$  in **Eq. (22)**). Notice that the dynamic variables  $\{\mathbf{x}_t^{(e)}\}$ ,  $e = 1, \dots, E$ , can be estimated separately for each epoch as these are independent measurements, and then we can condition over the shared connectivity matrices, or more conveniently by modifying the **Eq. (17)** as

$$\hat{\mathbf{X}}_{1:E}^{(i+1)} = \left( \mathbf{D}_L^T \mathbf{D}_L \otimes \mathbf{B}^T \mathbf{B} + \lambda (\mathbf{I}_{TN} - \mathbf{W})^T (\mathbf{I}_{TN} - \mathbf{W}) \right)^{-1} (\mathbf{D}_L^T \mathbf{D}_L \otimes \mathbf{I}_N) \mathbf{Z}_{1:E} \quad (24)$$

where  $\widehat{\mathbf{X}}_{1:E}^{(i+1)} = [\widehat{\mathbf{X}}_V^{(i+1,e=1)}, \dots, \widehat{\mathbf{X}}_V^{(i+1,e=E)}]$  and  $\mathbf{Z}_{1:E} = [\text{vec}(\mathbf{B}^T \mathbf{Y}^{(e=1)}), \dots, \text{vec}(\mathbf{B}^T \mathbf{Y}^{(e=E)})]$  (matrices  $\widehat{\mathbf{X}}_{1:E}^{(i+1)}$  and  $\mathbf{Z}_{1:E}$  are both of  $NT \times E$  dimensions). This trick has tremendous computational advantages as the inverse of the  $NT \times NT$  matrix is the most expensive operation. Whereas **Eq. (24)** keeps the same inverse matrix order as in **Eq. (17)**, on the other hand, the number of samples can be increased considerably by generating a higher number of epochs without significantly increasing the computational time.

**Extended Data Table 3:** For the lag=1 simulation for  $\sigma_o = 1$ , from left to right are shown the ground truth, the solution based on the  $\lambda$ 's theoretical value, and the regularised solutions obtained using the values of the hyperparameters found with the line- and plane-search cross-validation procedures.

| Ground truth   | SGD: $\lambda$ 's theoretical value                                  | SGD: $\lambda = 0.14$   | SGD: $\lambda \approx 0.67, \lambda_2 = 60.5$                        |
|--|--|---|--|
| $\begin{pmatrix} -0.5 & 0 \\ 0.7 & -0.5 \end{pmatrix}$ | $\begin{pmatrix} -0.4849 & -0.0064 \\ 5.3297 & 0.0520 \end{pmatrix}$ | $\begin{pmatrix} -0.4853 & -0.0038 \\ 0.5605 & -0.3273 \end{pmatrix}$ | $\begin{pmatrix} -0.3426 & 0.0585 \\ 0.7171 & -0.4171 \end{pmatrix}$ |

**Extended Data Table 4:** SSGD solution for one replication of the lag=1,2,3 small-scale simulation introduced above to evaluate the effect of fitting MPSS models for the noisier scenarios. (I) For the  $\sigma_o = 0.5$ , from top to bottom, are shown the estimated autoregressive coefficients for the fitted MPSS models that were obtained by exploring the hyperparameter for the subspaces  $\{(\lambda, \lambda_2^{(a)}, \lambda_1^{(a)}) \mid \lambda \geq 0, \lambda_2^{(a)} \geq 0, \lambda_1^{(a)} \geq 0\}$ ,  $\{(\lambda, \lambda_2^{(a)}) \mid \lambda \geq 0, \lambda_2^{(a)} \geq 0\}$ , and  $\{(\lambda, \lambda_1^{(a)}) \mid \lambda \geq 0, \lambda_1^{(a)} \geq 0\}$ , in this order. We use the hyperparameter values shown in **Fig. 3**. (II) Same as above but for the  $\sigma_o = 1$  scenario.

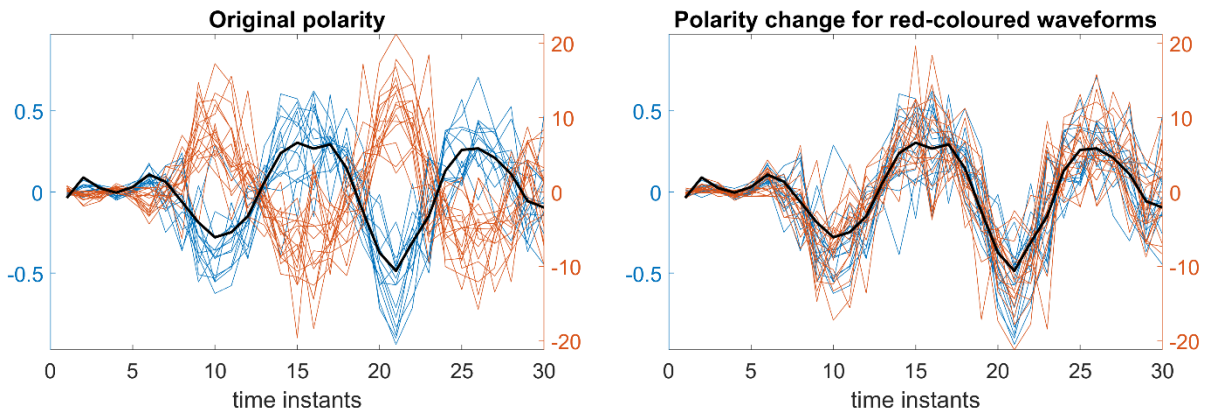
| I) Autoregressive coefficients estimated for the $\sigma_o = 0.5$ case |  |
|--|--|
| $\lambda, \lambda_2^{(a)}, \lambda_1^{(a)}$                            | $\mathbf{A} = \left\{ \begin{pmatrix} -0.94 & 0.06 & 0 \\ -0.23 & 1.07 & 0 \\ 0 & -0.07 & -1.49 \end{pmatrix}, \begin{pmatrix} -0.7 & 0 & 0 \\ 0.79 & -0.15 & 0 \\ 0 & 0 & -0.71 \end{pmatrix}, \begin{pmatrix} 0 & -0.07 & 0 \\ 0 & -0.24 & -0.02 \\ -0.39 & -0.04 & 0.01 \end{pmatrix} \right\}$                                       |
| $\lambda, \lambda_2^{(a)}$   | $\mathbf{A} = \left\{ \begin{pmatrix} -0.84 & 0.07 & -0.04 \\ -0.38 & 1.03 & 0.08 \\ 0 & -0.29 & -1.24 \end{pmatrix}, \begin{pmatrix} -0.57 & 0.04 & -0.07 \\ 0.56 & -0.12 & 0.11 \\ -0.04 & 0.35 & -0.34 \end{pmatrix}, \begin{pmatrix} 0.12 & -0.13 & -0.04 \\ -0.21 & -0.23 & 0.02 \\ -0.20 & -0.20 & 0.20 \end{pmatrix} \right\}$    |
| $\lambda, \lambda_1^{(a)}$   | $\mathbf{A} = \left\{ \begin{pmatrix} -0.93 & 0.03 & 0 \\ -0.20 & 1.07 & 0 \\ 0 & -0.06 & -1.50 \end{pmatrix}, \begin{pmatrix} -0.71 & 0 & 0 \\ 0.81 & -0.15 & 0 \\ 0 & 0 & -0.73 \end{pmatrix}, \begin{pmatrix} 0 & -0.06 & 0 \\ 0 & -0.23 & -0.02 \\ -0.39 & -0.02 & 0 \end{pmatrix} \right\}$   |
| II) Autoregressive coefficients estimated for the $\sigma_o = 1$ case  |  |
| $\lambda, \lambda_2^{(a)}, \lambda_1^{(a)}$                            | $\mathbf{A} = \left\{ \begin{pmatrix} -0.89 & 0 & -0.03 \\ -0.29 & 1.02 & 0 \\ 0 & 0 & -1.18 \end{pmatrix}, \begin{pmatrix} -0.71 & 0 & 0 \\ 0.61 & 0 & 0 \\ 0 & 0 & -0.13 \end{pmatrix}, \begin{pmatrix} 0 & 0 & 0 \\ 0 & -0.33 & 0 \\ -0.59 & -0.09 & 0.35 \end{pmatrix} \right\}$   |
| $\lambda, \lambda_2^{(a)}$   | $\mathbf{A} = \left\{ \begin{pmatrix} -0.67 & 0.05 & -0.03 \\ -0.40 & 0.89 & 0.03 \\ 0.08 & -0.26 & -1.06 \end{pmatrix}, \begin{pmatrix} -0.41 & 0.09 & -0.01 \\ 0.46 & 0.09 & -0.03 \\ 0.01 & 0.36 & -0.02 \end{pmatrix}, \begin{pmatrix} 0.27 & -0.16 & -0.01 \\ -0.11 & -0.34 & -0.06 \\ -0.27 & -0.23 & 0.38 \end{pmatrix} \right\}$ |
| $\lambda, \lambda_1^{(a)}$   | $\mathbf{A} = \left\{ \begin{pmatrix} -0.96 & 0 & -0.02 \\ 0 & 1.17 & 0 \\ 0 & 0 & -1.56 \end{pmatrix}, \begin{pmatrix} -0.75 & 0 & 0 \\ 0.97 & -0.24 & 0 \\ 0 & 0 & -0.78 \end{pmatrix}, \begin{pmatrix} 0 & -0.06 & 0 \\ 0 & -0.20 & 0 \\ -0.45 & 0 & 0 \end{pmatrix} \right\}$  |

**Extended Data Table 5:** For the lag=1 small-scale simulation, from left to right, are shown the ground truth and the estimated autoregressive coefficients for the different simulated SNR levels. The solutions are based on Matlab R2022a's functions `ssm` (top row) and `bssm` (bottom row), which implement a standard and Bayesian estimation of state-space models (cite). For each solution, the measured computational time is shown at the left side of each row. For each solution, the measured computational time is shown at the left side of each row.

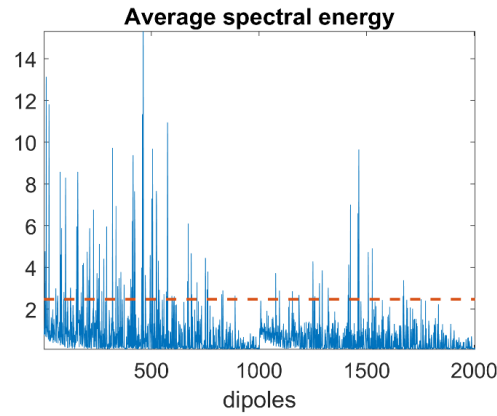
| Ground truth   | ssm: $\sigma_o = 0.1$ ; 7 sec  | ssm: $\sigma_o = 0.5$ ; 43 sec  | ssm: $\sigma_o = 1$ ; 14 sec  |
|--|--|---|---|
| $\begin{pmatrix} -0.5 & 0 \\ 0.7 & -0.5 \end{pmatrix}$ | $\begin{pmatrix} -0.4873 & 0.0138 \\ 0.7352 & -0.4015 \end{pmatrix}$ | $\begin{pmatrix} -0.5040 & 0.0106 \\ 0.7050 & -0.3948 \end{pmatrix}$  | $\begin{pmatrix} -0.4926 & 0.0284 \\ 0.6607 & -0.3991 \end{pmatrix}$  |
|  | <b>bssm: <math>\sigma_o = 0.1</math>; 19 sec</b>                     | <b>bssm: <math>\sigma_o = 0.5</math>; 18 sec</b>                      | <b>bssm: <math>\sigma_o = 1</math>; 19 sec</b>                        |
|  | $\begin{pmatrix} -0.4968 & 0.0014 \\ 0.7427 & -0.4071 \end{pmatrix}$ | $\begin{pmatrix} -0.5064 & -0.0032 \\ 0.7034 & -0.3939 \end{pmatrix}$ | $\begin{pmatrix} -0.5025 & -0.0123 \\ 0.6888 & -0.3928 \end{pmatrix}$ |

**Extended Data Table 6:** For the lag=1,2,3 small-scale simulation, from top to bottom, are shown the ground truth and the estimated autoregressive coefficients for the different simulated SNR levels. The solutions are based on Matlab R2022a's functions `ssm` (top row) and `bsm` (bottom row), which implement a standard and Bayesian estimation of state-space models (cite). For each solution, the measured computational time is shown at the left side of each row.

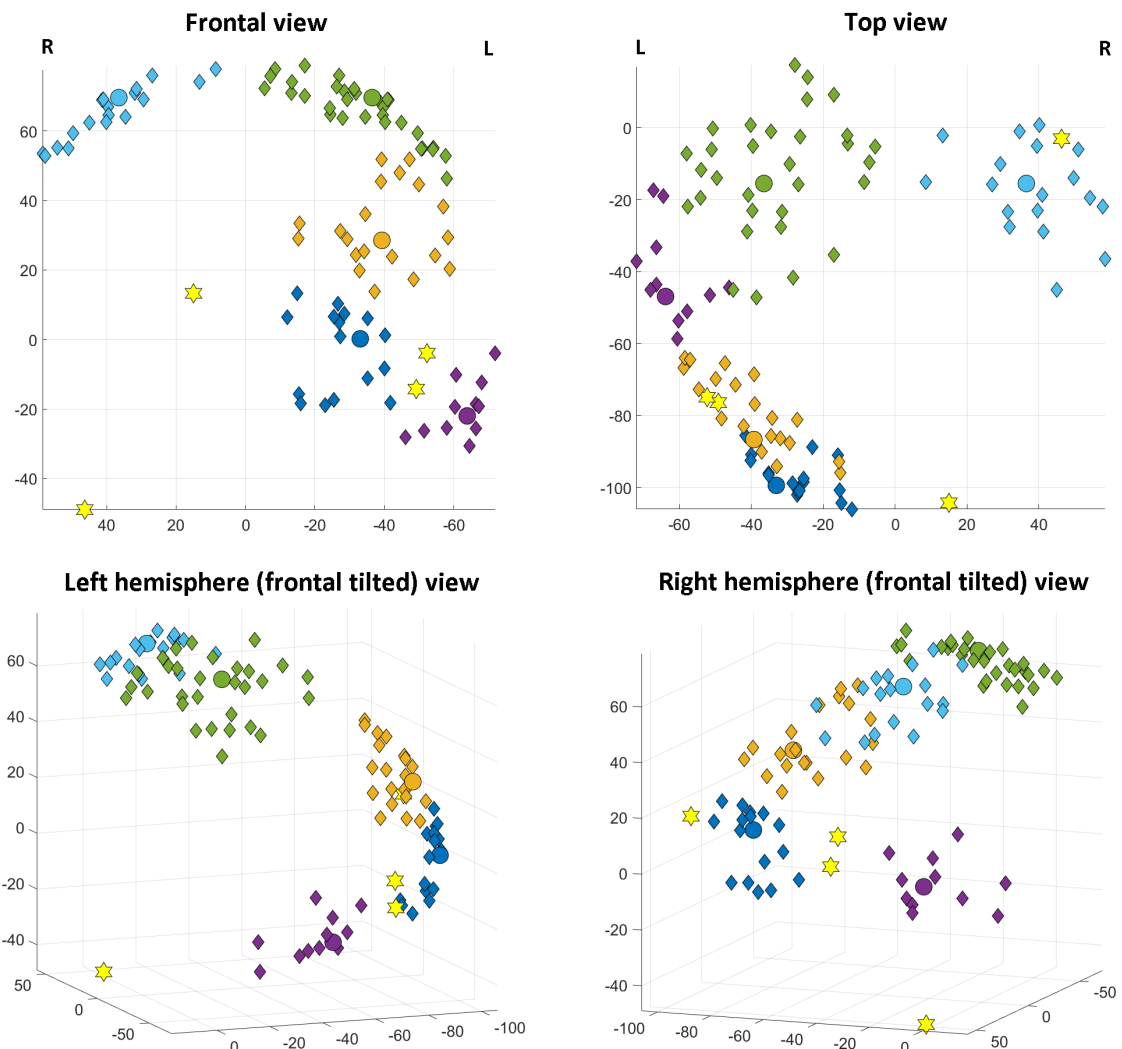
| I) Ground-truth autoregressive coefficients  |   |
|--|---|
| $\mathbf{A} = \left\{ \begin{pmatrix} -0.900 & 0 & 0 \\ -0.356 & 1.2124 & 0 \\ 0 & -0.3098 & -1.3856 \end{pmatrix}, \begin{pmatrix} -0.81 & 0 & 0 \\ 0.7136 & -0.49 & 0 \\ 0 & 0.5 & -0.64 \end{pmatrix}, \begin{pmatrix} 0 & 0 & 0 \\ -0.356 & 0 & 0 \\ 0 & -0.3098 & 0 \end{pmatrix} \right\}$ |   |
| II) State-space estimation with Matlab R2022a functions <code>ssm</code> and <code>ssm.estimate</code>   |   |
| $\sigma_o = 0.1$<br>64 sec   | $\mathbf{A} = \left\{ \begin{pmatrix} -1.03 & 0.10 & -0.06 \\ -0.43 & 1.20 & 0.09 \\ -0.09 & -0.37 & -1.36 \end{pmatrix}, \begin{pmatrix} -0.80 & -0.05 & -0.11 \\ 0.63 & -0.37 & 0.14 \\ -0.10 & 0.50 & -0.57 \end{pmatrix}, \begin{pmatrix} -0.11 & -0.04 & -0.07 \\ -0.36 & -0.13 & 0.05 \\ -0.08 & -0.29 & 0.06 \end{pmatrix} \right\}$ |
| $\sigma_o = 0.5$<br>59 sec   | $\mathbf{A} = \left\{ \begin{pmatrix} -1.12 & 0.10 & -0.03 \\ -0.28 & 1.10 & 0.07 \\ -0.11 & -0.35 & -1.24 \end{pmatrix}, \begin{pmatrix} -0.92 & -0.05 & -0.05 \\ 0.68 & -0.22 & 0.11 \\ -0.12 & 0.48 & -0.36 \end{pmatrix}, \begin{pmatrix} -0.22 & -0.05 & -0.04 \\ -0.20 & -0.19 & 0.03 \\ -0.17 & -0.29 & 0.18 \end{pmatrix} \right\}$ |
| $\sigma_o = 1$<br>115 sec  | $\mathbf{A} = \left\{ \begin{pmatrix} 0.90 & -1.91 & -1.07 \\ 1.40 & -2.58 & 0.08 \\ -1.62 & 4.86 & 0.64 \end{pmatrix}, \begin{pmatrix} 0.48 & -0.31 & 0.07 \\ 0.52 & -3.12 & -0.75 \\ -0.73 & -0.52 & -0.34 \end{pmatrix}, \begin{pmatrix} 0.98 & -2.19 & 0.58 \\ -0.82 & 2.29 & -0.51 \\ -1.82 & 4.61 & -0.81 \end{pmatrix} \right\}$     |
| III) State-space estimation with Matlab R2022a function <code>bsm</code> and <code>bsm.estimate</code>   |   |
| $\sigma_o = 0.1$<br>151 sec  | $\mathbf{A} = \left\{ \begin{pmatrix} -1.03 & 0.10 & -0.06 \\ -0.43 & 1.20 & 0.09 \\ -0.09 & -0.37 & -1.36 \end{pmatrix}, \begin{pmatrix} -0.80 & -0.05 & -0.11 \\ 0.63 & -0.36 & 0.14 \\ -0.11 & 0.50 & -0.57 \end{pmatrix}, \begin{pmatrix} -0.11 & -0.04 & -0.06 \\ -0.35 & -0.13 & 0.05 \\ -0.08 & -0.29 & 0.05 \end{pmatrix} \right\}$ |
| $\sigma_o = 0.5$<br>157 sec  | $\mathbf{A} = \left\{ \begin{pmatrix} -1.11 & 0.10 & -0.03 \\ -0.27 & 1.08 & 0.07 \\ -0.11 & -0.32 & -1.26 \end{pmatrix}, \begin{pmatrix} -0.91 & -0.05 & -0.05 \\ 0.69 & -0.20 & 0.11 \\ -0.12 & 0.43 & -0.40 \end{pmatrix}, \begin{pmatrix} -0.21 & -0.05 & -0.04 \\ -0.18 & -0.20 & 0.03 \\ -0.20 & -0.26 & 0.16 \end{pmatrix} \right\}$ |
| $\sigma_o = 1$<br>323 sec  | $\mathbf{A} = \left\{ \begin{pmatrix} -1.26 & 0.16 & 0 \\ -0.10 & 1.16 & -0.01 \\ -0.14 & -0.42 & -1.07 \end{pmatrix}, \begin{pmatrix} -1.11 & -0.14 & 0.02 \\ 0.73 & -0.30 & 0.04 \\ -0.10 & 0.66 & -0.09 \end{pmatrix}, \begin{pmatrix} -0.44 & -0.03 & 0 \\ -0.22 & -0.15 & -0.01 \\ -0.12 & -0.39 & 0.34 \end{pmatrix} \right\}$        |



**Extended Data Figure 1:** Manually correction of the polarity for the estimated waveforms of the 100 most salient dipoles. This operation is illustrated for the estimated solution corresponding to the fourth ground-truth source, the same subplot shown in Fig. 5C, fourth row, and seventh column. **Left side:** original waveforms as estimated by HGDALS. **Right side:** after manually correcting the polarity for the waveform in red color. In both cases, the black curve represents the ground-truth waveform for the simulated source.



**Extended Data Figure 2:** Average spectral energy calculated from the estimated time series  $\{x_t^{(e)}\}$ ,  $e = 1, \dots, E$ , by calculating their Fourier transform and averaging from the second to sixth spectral component across epochs. The dipoles in the plot's left (right) side are located in the left (right) hemisphere. The threshold (red discontinuous) line indicates the lower limit corresponding to selected 100 most salient dipoles.



**Extended Data Figure 3:** Correspondingly to Fig. 5B in the main text, removing the brain cortical surface and leaving only the ground-truth sources (colored sphere points) and estimated (colored diamond points) dipoles. The simulated dipoles are located in the following brain regions: left-hemisphere occipital lobe (blue), convergence between left hemisphere parietal and occipital lobes (orange), inferior temporal lobe (purple), and left/right (green/cyan) hemispheres somatosensory cortices. Estimated outlier dipoles are highlighted with yellow star points. Using different views for the same locations highlights the clustering characteristics of estimated dipoles, i.e., revealing that they are located closely around each of their corresponding simulated ground-truth sources.

**Extended Data Table 7:** Matlab R2022a code for a standard solution of a state-space model with “*ssm.estimate*”. Evaluate the solution for different SNR values by changing the value of “*so*” in lines 8-10. The code for function “*mvarlsim1*”, for bivariate with lag=1 simulation, is provided in **Extended Data Table 8**. Nearby initial values for the parameters are provided with “*params0*”, in line 30. Logically, the lower bound parameter “*lowBound*” (line 31) sets 0 for covariance variables. Uncomment lines 33-34 and comment lines 35-36 to try with different optimization settings.

```

1. % test_ssm_M5T200N2P1
2. rng('default');
3.
4. %% Simulation
5. Nepoch = 1;
6. ss = 1;
7.
8. so = 0.1;
9. % so = 0.5;
10. % so = 1;
11.
12. M = 5;
13. T = 200;
14. [x, y, A, B] = mvarlsim1(M, T, Nepoch, ss, so);
15. N = size(B,2);
16. p = size(A,3);
17.
18. figure;
19. subplot 211;
20. plot(x', 'LineWidth', 2); axis tight; set(gca, 'FontSize', 24);
21. legend('1','2');
22. ylabel('\boldmath\mathrm{X}$', 'Interpreter', 'latex');
23.
24. %% Estimate with Matlab Econometric Toolbox
25. At = [NaN NaN; NaN NaN];
26. Bt = [NaN 0; 0 NaN];
27. Ct = B;
28. Dt = [NaN 0 0 0 0; 0 NaN 0 0 0; 0 0 NaN 0 0; 0 0 0 NaN 0; 0 0 0 0 NaN];
29. Mdl = ssm(At, Bt, Ct, Dt, 'Mean0', 0, 'Cov0', 10*eye(N), 'StateType', zeros(N,1));
30. params0 = 0.1*ones(11,1);
31. lowBound = [-Inf(4,1); zeros(N+M,1)];
32.
33. % options = optimoptions(@fmincon, 'ConstraintTolerance', 1e-6, ...
34. % 'Algorithm', 'sqp', 'MaxFunctionEvaluations', 10000);
35. options = optimoptions(@fmincon, 'ConstraintTolerance', 1e-6, ...
36. % 'Algorithm', 'interior-point', 'MaxFunctionEvaluations', 10000);
37.
38. tic
39. EstMdl = estimate(Mdl, y', params0, 'lb', lowBound, 'Options', options)
40. toc

```

**Extended Data Table 8:** Matlab function “*mvarlsim1*” which generates the bivariate lag=1 simulation in our analysis.

```

1. function [x, y, A, B] = mvarlsim1(M, T, Nepoch, ss, so)
2. N = 2;
3. P = 1;
4. A = [-0.5 0; 0.7 -0.5];
5. assert(N == size(A,1));
6. assert(N == size(A,2));
7. assert(P == size(A,3));
8.
9. % generate state data: x
10. x = ss*randn(N,Nepoch,T);
11. for t = P+1:T
12.     x(:, :, t) = x(:, :, t) + A*x(:, :, t-1);
13. end
14.
15. % generate observation data: y
16. B = rand(M,N);
17. % B = B/diag(sqrt(sum(B.^2)));
18. y = B*reshape(x,N,[],) + so*randn(M,Nepoch*T);
19. y = reshape(y, [M Nepoch T]);
20.
21. % rearrange so that epochs are in the 3rd dimension
22. x = permute(x, [1 3 2]);
23. y = permute(y, [1 3 2]);

```

**Extended Data Table 9:** Similar to **Extended Data Table 7** but for the three-variate lag=1,2,3 simulation with function “*mvar3sim1*”, which is provided in **Extended Data Table 10**. Nearby initial values for the parameters are provided with “*params0*”, in line 31. Logically, the lower bound parameter “*lowBound*” (line 32) sets 0 for covariance variables. Notice that values in “*lowBound*” and “*upBound*” are restricted (lines 32-33) to avoid disparate parameter values. Uncomment lines 35-36 and comment lines 37-38 to try with different optimization settings. Likewise, uncomment line 41 and comment line 42 to play with the results.

```

1. % test_ssm_M5T240N3P3
2. rng('default');
3.
4. %% Simulation
5. Nepoch = 1;
6. ss = 1;
7.
8. so = 0.1;
9. % so = 0.5;
10. % so = 1;
11.
12. M = 5;
13. Fs = 120;
14. T = 2*Fs;
15. [x, y, A, B] = mvar3sim1(M, Fs, T, Nepoch, ss, so);
16. N = size(B,2);
17. p = size(A,3);
18.
19. figure;
20. subplot 211;
21. plot(x', 'LineWidth', 2); axis tight; set(gca, 'FontSize', 24);
22. legend('1', '2', '3');
23. ylabel('\boldmath\mathrm{X}$', 'Interpreter', 'latex');
24.
25. %% Estimate with Matlab Econometric Toolbox
26. At = [NaN(N) NaN(N) NaN(N); eye(N) zeros(N) zeros(N); zeros(N) eye(N) zeros(N)];
27. Bt = [diag(NaN(N,1)); zeros(N); zeros(N)];
28. Ct = [B zeros(M,N) zeros(M,N)];
29. Dt = diag(NaN(M,1));
30. Mdl = ssm(At, Bt, Ct, Dt, 'Mean0', 0, 'Cov0', 0.1*eye(3*N), 'StateType', zeros(3*N,1));
31. params0 = 0.1*ones(35,1);
32. lowBound = [-5*ones(35-N-M,1); zeros(N+M,1)];
33. upBound = [5*ones(35-N-M,1); 5*ones(N+M,1)];
34.
35. % options = optimoptions(@fmincon, 'ConstraintTolerance', 1e-6, ...
36. % 'Algorithm', 'sqp', 'MaxFunctionEvaluations', 10000);
37. options = optimoptions(@fmincon, 'ConstraintTolerance', 1e-6, ...
38. % 'Algorithm', 'interior-point', 'MaxFunctionEvaluations', 10000);
39.
40. tic
41. % EstMdl = estimate(Mdl, y', params0, 'lb', lowBound, 'Options', options)
42. EstMdl = estimate(Mdl, y', params0, 'lb', lowBound, 'ub', upBound, 'Options', options)
43. toc

```

**Extended Data Table 10:** Matlab function “*mvar3sim1*” which generates the three-variate lag=1,2,3 simulation.

```

1. function [x, y, A, B] = mvar3sim1(M, Fs, T, Nepoch, ss, so)
2. % Fs = 120; % sampling frequency is 120 Hz
3. % T = 2*Fs; % 2 seconds simulation
4. r = [0.9 0.7 0.8];
5. f = [40 10 50];
6. dt = 1/Fs;
7. theta = 2*pi*f*dt;
8.
9. N = 3; % number of nodes
10. p = 3; % true order of the MVAR model
11. A = zeros(N,N,p);
12. A(:, :, 1) = diag(2*r.*cos(theta)) + [0 0 0; -0.356 0 0; 0 -0.3098 0];
13. A(:, :, 2) = diag(-r.^2) + [0 0 0; 0.7136 0 0; 0 0.5 0];
14. A(:, :, 3) = [0 0 0; -0.356 0 0; 0 -0.3098 0];
15. assert(N == size(A,1));
16. assert(N == size(A,2));
17. assert(p == size(A,3));
18.
19. % generate state data: x
20. x = ss*randn(N,Nepoch,T);
21. for t = p+1:T

```

```

22.     for k = 1:p
23.         x(:, :, t) = x(:, :, t) + A(:, :, k)*x(:, :, t-k);
24.     end
25. end
26.
27. % generate observation data: y
28. B = rand(M,N);
29. y = B*reshape(x,N, []) + so*randn(M,Nepoch*T);
30. y = reshape(y, [M Nepoch T]);
31.
32. % rearrange so that epochs are in the 3rd dimension
33. x = permute(x, [1 3 2]);
34. y = permute(y, [1 3 2]);

```

**Extended Data Table 11:** Matlab R2022a code for a Bayesian solution of a state-space model with “*bssm.estimate*”, for the bivariate lag=1 simulation. Evaluate the solution for different SNR values by changing the value of “*so*” in lines 8-10. Check related information in the caption of **Extended Data Table 7**. Notice that the same model specified above in standard form is converted to the corresponding Bayes form with the function “*ssm2bssm*” (line 31). As can be seen, for the Bayesian estimation, there is no need to used boundary conditions for the parameters estimation. However, the solution may be sensitive for different initial parameter values, particularly for low SNR simulations, change “*params0*” in line 33 to check.

```

1. % test_bssm_M5T200N2P1
2. rng('default');
3.
4. %% Simulation
5. Nepoch = 1;
6. ss = 1;
7.
8. so = 0.1;
9. % so = 0.5;
10. % so = 1;
11.
12. M = 5;
13. T = 200;
14. [x, y, A, B] = mvar1siml(M, T, Nepoch, ss, so);
15. N = size(B,2);
16. p = size(A,3);
17.
18. figure;
19. subplot(2,1);
20. plot(x, 'LineWidth', 2); axis tight; set(gca, 'FontSize', 24);
21. legend('1','2');
22. ylabel('\boldmath{\mathrm{X}}$', 'Interpreter', 'latex');
23.
24. %% Estimate with Matlab Econometric Toolbox
25. At = [NaN NaN; NaN NaN];
26. Bt = [NaN 0; 0 NaN];
27. Ct = B;
28. Dt = [NaN 0 0 0 0; 0 NaN 0 0 0; 0 0 NaN 0 0; 0 0 0 NaN 0; 0 0 0 0 NaN];
29. Mdl = ssm(At, Bt, Ct, Dt, 'Mean0', 0, 'Cov0', 10*eye(N), 'StateType', zeros(N,1));
30.
31. bayesMdl = ssm2bssm(Mdl);
32.
33. params0 = 0.1*ones(11,1);
34. options = optimoptions(@fminunc, 'OptimalityTolerance', 1e-6, ...
35.     'MaxFunctionEvaluations', 1e4);
36.
37. tic
38. EstPostMdl = estimate(bayesMdl, y', params0, 'Options', options)
39. toc

```

**Extended Data Table 12:** Matlab R2022a code for a Bayesian solution of a state-space model with “*bssm.estimate*”, for the three-variate lag=1,2,3 simulation. Check related information in the caption of the tables for previous codes. Notice that the same model specified above in standard form is converted to the corresponding Bayes form with the function “*ssm2bssm*” (line 32). As can be seen, for the Bayesian estimation, there is no need to used boundary conditions for the parameters estimation. However, the solution may be sensitive for different initial parameter values, particularly for low SNR simulations, change “*params0*” in line 33 to check.

```

1. % test_bssm_M5T240N3P3
2. rng('default');
3.
4. %% Simulation

```



```

5. Nepoch = 1;
6. ss = 1;
7.
8. so = 0.1;
9. % so = 0.5;
10. % so = 1;
11.
12. M = 5;
13. Fs = 120;
14. T = 2*Fs;
15. [x, y, A, B] = mvar3sim1(M, Fs, T, Nepoch, ss, so);
16. N = size(B,2);
17. p = size(A,3);
18.
19. figure;
20. subplot 211;
21. plot(x', 'LineWidth', 2); axis tight; set(gca, 'FontSize', 24);
22. legend('1', '2', '3');
23. ylabel('\boldmath\mathrm{X}', 'Interpreter', 'latex');
24.
25. %% Estimate with Matlab Econometric Toolbox
26. At = [NaN(N) NaN(N) NaN(N); eye(N) zeros(N) zeros(N); zeros(N) eye(N) zeros(N)];
27. Bt = [diag(NaN(N,1)); zeros(N); zeros(N)];
28. Ct = [B zeros(M,N) zeros(M,N)];
29. Dt = diag(NaN(M,1));
30. Mdl = ssm(At, Bt, Ct, Dt, 'Mean0', 0, 'Cov0', 0.1*eye(3*N), 'StateType', zeros(3*N,1));
31.
32. bayesMdl = ssm2bssm(Mdl);
33.
34. params0 = 0.1*ones(35,1);
35. options = optimoptions(@fminunc, 'OptimalityTolerance', 1e-6, ...
36.     'MaxFunctionEvaluations', 1e5);
37.
38. tic
39. EstPostMdl = estimate(bayesMdl, y', params0, 'Options', options)
40. toc

```